

Dynamics and non-integrability of the double spring pendulum

Wojciech Szumiński^{1*}

¹*Institute of Physics, University of Zielona Góra, Licealna 9, PL-65-407, Zielona Góra, Poland*

Andrzej J. Maciejewski²

²*Janusz Gil Institute of Astronomy, University of Zielona Góra, Licealna 9, PL-65-407, Zielona Góra, Poland*

Abstract

This paper investigates the dynamics and integrability of the double spring pendulum, which has great importance in studying nonlinear dynamics, chaos, and bifurcations. Being a Hamiltonian system with three degrees of freedom, its analysis presents a significant challenge. To gain insight into the system's dynamics, we employ various numerical methods, including Lyapunov exponents spectra, phase-parametric diagrams, and Poincaré cross-sections. The novelty of our work lies in the integration of these three numerical methods into one powerful tool. We provide a comprehensive understanding of the system's dynamics by identifying parameter values or initial conditions that lead to hyper-chaotic, chaotic, quasi-periodic, and periodic motion, which is a novel contribution in the context of Hamiltonian systems. In the absence of gravitational potential, the system exhibits S^1 symmetry, and the presence of an additional first integral was identified using Lyapunov exponents diagrams. We demonstrate the effective utilization of Lyapunov exponents as a potential indicator of first integrals and integrable dynamics. The numerical analysis is complemented by an analytical proof regarding the non-integrability of the system. This proof relies on the analysis of properties of the differential Galois group of variational equations along specific solutions of the system. To facilitate this analysis, we utilized a newly developed extension of the Kovacic algorithm specifically designed for fourth-order differential equations. Overall, our study sheds light on the intricate dynamics and integrability of the double spring pendulum, offering new insights and methodologies for further research in this field.

Keywords: Variable-length pendulum; Double spring pendulum; Ordinary differential equations; Chaos in Hamiltonian systems; Numerical simulation; Integrability analysis

Declaration. The article has been published in [1], and the final version is available at:
<https://doi.org/10.1016/j.jsv.2024.118550>

1. Introduction and motivation

The dynamics of various types of pendulums have a long history in mechanics and physics. Since the time of Galileo Galilei, analysis of their complicated behavior is still in great scientific activity. It is caused by the simplicity of these systems and by many fundamental and not obvious phenomena exhibited by pendulums. Indeed, one can find numerous papers, books, and video clips concerning their non-linear and chaotic dynamics. To exemplify it, let us mention the paradigm models such as the spring pendulum [2–6], the magnetic pendulum [7–9], the double and the triple pendulums [10–19], the coupled pendulums [20–24] and the swinging Atwood machine [25–29]. These models have been extensively studied by researchers both theoretically and practically [29–35]. In fact, pendulum systems have many potential applications [36–39]. For instance, multiple pendulum models play a crucial role in engineering and in synchronization theory [40–43]. Analyzing the dynamics of the double pendulum system helps engineers design control algorithms, especially for bipedal robots

Email addresses: w.szuminski@if.uz.zgora.pl (Wojciech Szumiński^{1*}), a.maciejewski@ia.uz.zgora.pl (Andrzej J. Maciejewski²)

where motion stability is a critical aspect [44, 45]. However, a simple spring pendulum can be treated as a classical analog of the quantum phenomenon of Fermi resonance in the infrared spectrum of carbon dioxide [46, 47], and currently it has been treated as a system with potential applications in atmosphere modeling [48–50].

Dynamics and integrability analysis of pendulum-like systems with three or more degrees of freedom have not yet been fully explored. This is for several reasons. Namely, for Hamiltonian systems with two degrees of freedom, an essential tool for giving a quick insight into the system dynamics is the so-called Poincaré cross-sections method. This technique by a simple cross-sections of the phase curves with a two-dimensional plane shows the coexistence of periodic, quasi-periodic, and chaotic orbits at the section plane giving a qualitative insight into system dynamics. However, for Hamiltonian systems with more than two degrees of freedom, this method is less practical. One significant issue arises from the fact that the intersections of trajectories with a Poincaré section hyperplane which is of dimension higher than two. This complicates the extraction of meaningful information, as the resulting section may exhibit intricate and convoluted structures that are difficult to interpret. Moreover, higher dimensionality introduces additional complexities, such as the presence of more intricate bifurcation scenarios and a richer set of possible trajectories.

On the other hand, computations of Lyapunov exponents provide a quantitative description of chaos and its strength and can be effectively applied to a system with many degrees of freedom. The analysis of the nontrivial exponent values provides valuable information, such as the presence of new isolating integrals. However, in a regular regime, where all exponents are zero, periodic and quasi-periodic solutions are not distinguishable. Therefore, in a recent article [24], the authors combined these two methods by providing compressive information on the dynamics of a model considered.

Nevertheless, the integrability analysis of pendulum-like systems is difficult due to their dependence on several parameters, such as lengths of pendulum arms, masses of bobs, spring stiffness, gravity acceleration, etc. Therefore, to perform a complete integrability analysis of these models, one needs a powerful tool, which enables one to distinguish values of parameters for which a considered system is suspected to be integrable. Such an effective and strong tool is the so-called Morales–Ramis theory [51, 52]. Let us recall the main theorem of this theory.

Theorem 1.1 (Morales–Ramis (1999)). *If a Hamiltonian system is integrable in the sense of Liouville in a neighborhood of a particular solution, then the identity component of the differential Galois group of the variational equations along this solution is Abelian.*

The Morales-Ramis theory has already been successfully applied to various important physical systems [53–60] as well as non-Hamiltonian systems [56, 61–63], to cite just a few. Because of this, many new integrable and super-integrable systems were found [64–66]. To exemplify it, we mention two generalizations of the swinging Atwood machine model recently studied in [24, 28]. In this paper, the authors performed a detailed integrability analysis and found integrable and super-integrable cases with additional first integrals quadratic and quartic in the momenta. These first integrals were later used in constructions of general solutions of nonlinear equations of motions.

In most cases, however, the Morales-Ramis theory has been applied to Hamiltonian systems with two degrees of freedom for which a system of variational equations splits into two subsystems of linear equations. Next, each of these subsystems can be transformed (in general) into an equivalent second-order equation with rational coefficients. For such equations, there exists an algorithm called the Kovacic algorithm [67], which can be used to determine the differential Galois group properties of rationalized variational equations. For Hamiltonian systems with three degrees of freedom, the normal variational equations form a four-dimensional subsystem in most cases and the analysis of its differential Galois group is considerably more complicated. Unfortunately, there is no equivalent of the Kovacic algorithm for linear differential equations with rational coefficients of higher order, although many partial results are known [68, 69]. In recent work [70], the authors present an algorithm to study the differential Galois group for symplectic differential operators of dimension four, which is perhaps the most comprehensive study available. We will be using this algorithm in our considerations.

Currently, there is great activity studying variable-length pendulum systems, such as the swinging Atwood machine [27] and its generalizations [28], the variable-length coupled pendulums recently studied in [24], or the double variable-length pendulum with counterweight mass [71–73]. Variable-length pendulum systems are excellent examples for studying nonlinear dynamics, chaos, and bifurcations. Moreover, such models are interesting due to their potential physical applications in crane models and lifting equipment, where understanding motion and stability is crucial for safe and efficient operation [74–78], The flexibility and maneuverability of the

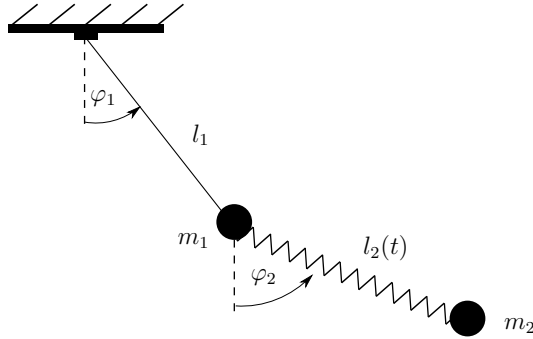


Figure 1: Geometry of the double spring pendulum. The system oscillates under the influence of the gravitational and Hooke's potentials. Here m_1 and m_2 are masses of the bobs, while l_1 and $l_2(t)$ are lengths of the pendulum's arms. The Lagrange function describing the model is defined in Eq. (2.3)

variable length pendulum system make it important in robotics, where dynamic stability is crucial [79–81]. Furthermore, the variable lengths pendulum systems have applications in energy conversion and storage, where swinging can be used to generate electricity [82–84].

Finally, studying the dynamics of variable length pendulum system can find its possible application in active debris removal missions [85–87]. One of the most promising models is a tethered tug-debris system. Usually, it consists of the mother satellite of mass m_1 moving in an unperturbed Kepler circular orbit and the sub-satellite of mass m_2 attached to the mother satellite through an elastic massless tether of length $l(t)$. Although active debris removal using a tethered tug-debris system is a relatively new topic, several books [88–90] and hundreds of scientific articles have been already published [90–93]. However, many aspects of this problem remain unexplored. For example, the equations governing the dynamics of tethered satellites are highly nonlinear. Hence the dynamical behavior is very rich and in some cases can be chaotic [94–96]. Because chaos in dynamical systems in space can be exceedingly dangerous, especially concerning the stability and predictability of artificial celestial body movements, it is crucial to detect values of parameters and initial conditions for which the motion of the system will be regular and predictable. Indeed, small changes in initial conditions or parameters can lead to drastically different trajectories along which the system will move.

The aim of this work is to perform a comprehensive analysis of the dynamics and integrability of the double-spring pendulum system, which can be regarded as a mathematical model of the tethered satellite system. Because the proposed model is a Hamiltonian system with three degrees of freedom, its analysis is quite challenging. The equations of motion obtained are strongly nonlinear and require careful numerical analysis to obtain reliable results. However, there is a lack of literature on its dynamics and integrability analysis. This is the main topic of this paper. To study their complex dynamics, we employ numerical methods such as Lyapunov exponent diagrams and phase-parametric diagrams. Moreover, for special cases, we use the Poincaré cross-section method. We join these three numerical techniques to get a complete insight into the dynamics of the considered models. For their exhaustive integrability analysis, we utilize the differential Galois theory and the Kovacic algorithm of dimension four.

The rest of the paper is organized as follows. In Sec. 2, we introduce the model under consideration and derive the corresponding equations of motion. In Sec. 3, we give a qualitative and quantitative description of its chaotic motion by joining numeral methods, such as Lyapunov's exponent spectra, phase-parametric diagrams, and Poincaré cross-sections. Next, in Sec. 4, we perform an effective integrability analysis of the model with the help of Morales–Ramis theory and the application of the Kovacic algorithm of dimension four. The proof of its non-integrability for all values of the parameters is given. The basic facts and theorems devoted to the integrability analysis of variational equations of dimension four are included in the appendix.

2. Description of the system

In Fig. 1 the geometry of the system is presented. We study the double spring pendulum system. It consists of a simple mathematical pendulum of mass m_1 and length l_1 and a weightless spring of length $l_2 = l_2(t)$ with a mass m_2 attached at its end. The system moves under the influence of the gravitational and Hooke's potential forces.

The Lagrange function of the system is as follows

$$\begin{aligned}
L &= T - V_g - V_k, \\
T &= \frac{1}{2}m_1 (\dot{x}_1^2 + \dot{y}_1^2) + \frac{1}{2}m_2 (\dot{x}_2^2 + \dot{y}_2^2), \\
V_g &= -gm_1x_1 - gm_2x_2, \\
V_k &= \frac{1}{2}k \left(\sqrt{(x_2 - x_1)^2 + (y_2 - y_1)^2} - l_{20} \right)^2
\end{aligned} \tag{2.1}$$

where $k \in \mathbb{R}^+$ is the Young modulus of the spring and l_{20} is its natural length. Following Fig. 1, we utilize the polar coordinates

$$\begin{aligned}
x_1(t) &= l_1 \cos \varphi_1(t), \\
y_1(t) &= l_1 \sin \varphi_1(t), \\
x_2(t) &= x_1(t) + l_2(t) \cos \varphi_2(t), \\
y_2(t) &= y_1(t) + l_2(t) \sin \varphi_2(t).
\end{aligned} \tag{2.2}$$

Hence, we obtain a system of three degrees of freedom defined by the Lagrange function

$$\begin{aligned}
L &= \frac{1}{2} (m_1 + m_2) l_1^2 \dot{\varphi}_1^2 + \frac{1}{2} m_2 \left(\dot{l}_2^2 + l_2^2 \dot{\varphi}_2^2 \right) + m_2 l_1 \dot{\varphi}_1 \left[l_2 \dot{\varphi}_2 \cos(\varphi_1 - \varphi_2) - \dot{l}_2 \sin(\varphi_1 - \varphi_2) \right], \\
&+ (m_1 + m_2) g l_1 \cos \varphi_1 - m_2 g l_2 \cos \varphi_2 - \frac{1}{2} k (l_2 - l_{20})^2.
\end{aligned} \tag{2.3}$$

To minimize the number of parameters and thus simplify our calculations as much as possible, we rescale $\ell(t) = l_2(t)/l_1$, and we introduce a new time as

$$t \rightarrow \omega_k^{-1} t, \quad \text{where} \quad \omega_k = \sqrt{\frac{k}{m_2}}. \tag{2.4}$$

The dimensionless form of Lagrangian (2.3) is as follows.

$$\begin{aligned}
L &= \frac{1}{2} \left(\dot{\ell}^2 + \ell^2 \dot{\varphi}_2^2 \right) + \frac{1}{2} (\mu + 1) \dot{\varphi}_1^2 + \ell \cos(\varphi_1 - \varphi_2) \dot{\varphi}_1 \dot{\varphi}_2 - \sin(\varphi_1 - \varphi_2) \dot{\ell} \dot{\varphi}_1 \\
&+ \omega [(\mu + 1) \cos \varphi_1 + \ell \cos \varphi_2] - \frac{(\delta - \ell)^2}{2}.
\end{aligned} \tag{2.5}$$

Here $\mu, \delta, \omega \in \mathbb{R}^+$ are dimensionless parameters defined as

$$\mu := \frac{m_1}{m_2}, \quad \delta := \frac{l_{20}}{l_1}, \quad \omega := \frac{\omega_g^2}{\omega_k^2}, \quad \text{where} \quad \omega_g = \sqrt{\frac{g}{l_1}}.$$

In our analysis, we will use only Lagrange variables. One can introduce canonical variables in order to use Hamilton's formalism directly; however, in canonical variables, the equations of motion are more complicated. We will use the following variables: the angular velocities $\omega_1 = \dot{\varphi}_1, \omega_2 = \dot{\varphi}_2$ and $v = \dot{\ell}$ instead of momenta. Hence, a set of three second-order Lagrange equations can be rewritten as a system of six first-order differential equations of the form

$$\begin{cases}
\dot{\ell} = v, \\
\dot{v} = \ell \omega_2^2 + \cos(\varphi_1 - \varphi_2) \omega_1^2 + \omega \cos \varphi_1 \cos(\varphi_1 - \varphi_2) + \frac{\delta - \ell}{2\mu} (1 + 2\mu - \cos[2(\varphi_1 - \varphi_2)]), \\
\dot{\varphi}_1 = \omega_1, \\
\dot{\omega}_1 = \frac{\delta - \ell}{\mu} \sin(\varphi_1 - \varphi_2) - \omega \sin \varphi_1, \\
\dot{\varphi}_2 = \omega_2, \\
\dot{\omega}_2 = \frac{1}{\ell} (\sin(\varphi_1 - \varphi_2) \omega_1^2 - 2v \omega_2) + \frac{1}{\ell} \left(\frac{\ell - \delta}{2} \sin[2(\varphi_1 - \varphi_2)] + \omega \cos \varphi_1 \cos(\varphi_1 - \varphi_2) \right).
\end{cases} \tag{2.6}$$

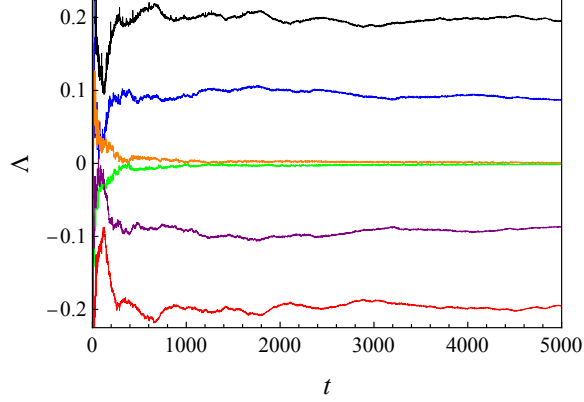


Figure 2: (Color online) The Lyapunov exponents spectrum $\Lambda = \{\lambda_1, \lambda_2, \lambda_3, \lambda_4, \lambda_5, \lambda_6\}$ of system (2.6), computed for the constant values of parameters (3.1) and initial condition (3.2). For a sufficient amount of time steps, the convergence of the Lyapunov exponents is ensured. Because two Lyapunov exponents are positive, the system reveals hyperchaotic dynamics

System (2.6) has the following energy first integral

$$E = \frac{1}{2} (\dot{l}^2 + \ell^2 \dot{\varphi}_2^2) + \frac{1}{2} (\mu + 1) \dot{\varphi}_1^2 + \ell \cos(\varphi_1 - \varphi_2) \dot{\varphi}_1 \dot{\varphi}_2 - \sin(\varphi_1 - \varphi_2) \ell \dot{\varphi}_1 - \omega [(\mu + 1) \cos \varphi_1 + \ell \cos \varphi_2] + \frac{(\delta - \ell)^2}{2}. \quad (2.7)$$

3. Numerical analysis

To visualize the dynamics of the system, we perform a numerical analysis with the help of Lyapunov's To visualize the dynamics of the system, we perform a numerical analysis with the help of Lyapunov's exponent diagrams (Lyapunov's diagrams in short), phase-parametric diagrams, and the Poincaré cross-sections method. In order, to get the most reliable results, we systematically join these three methods and we give a complete picture of the system's complex dynamics.

3.1. Diagrams of Lyapunov exponents

Lyapunov exponent is a measure of a system's predictability and sensitivity to changes in its initial conditions. Thus, it is commonly used in studying chaos in dynamical systems by quantifying the rate of exponential divergence of nearby trajectories in a phase space. According to chaos theory, if at least one Lyapunov exponent is positive, then a considered system is sensitive to changes in its initial conditions and chaotic phenomena appear. Moreover, if two or more Lyapunov exponents are positive, then the system is treated as the hyperchaotic one [97]. In our research, we use the standard algorithm introduced by Benettin et al. [98] to calculate two-parameter diagrams of the Lyapunov exponents. This technique is based on the integration of variational equations for n initial conditions with successive applications of the Gram-Schmidt orthonormalization procedure. In the presented study, we employ the standard algorithm implemented in Mathematica by Sandri [99]. However, in order to enhance the speed and precision of our results, we utilize the NDSolve solver with the "ExplicitRungeKutta" method instead of Euler's method. After conducting a thorough and detailed analysis, we select a period between re-orthonormalizations of $T = 1$, a maximum step size of $\tau = 0.01$, and a number of steps typically set to $k = 5000$ or more. The working precision for the entire numerical analysis is set to at least 12, ensuring the maintenance of precision up to 12 digits during internal computations. Moreover, the constancy of the energy first integral E , as given in (2.7), is utilized to verify the numerical integrations. We maintain both relative and absolute errors within the range of 10^{-11} . These chosen parameters facilitate the efficient computation of Lyapunov exponents, ensuring their robust convergence and enabling possible fast calculations.

Fig. 2 shows the Lyapunov exponents spectrum for system (2.6), computed for constant values of the parameters

$$\mu = 3, \quad \delta = 1, \quad \omega = 1, \quad (3.1)$$

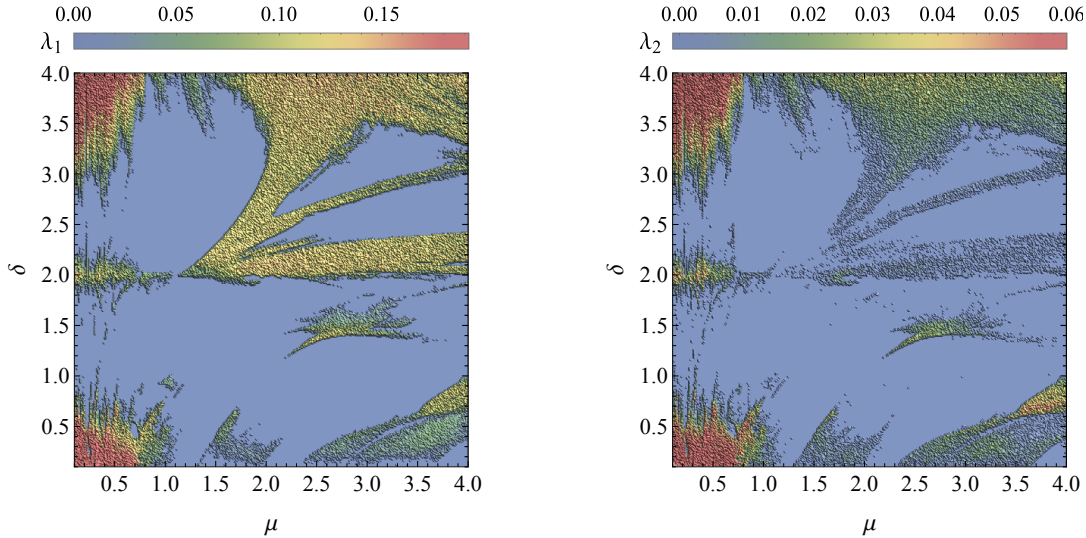


Figure 3: (Color online) The diagrams of two Lyapunov exponents λ_1 and λ_2 computed for the grid of 400×400 values of $\mu, \delta \in [0.1, 4]$ with $\omega = 1$. The numerical integrations were performed successively for the initial condition (3.2). Color scales are proportional to the magnitudes of λ_1 and λ_2 , respectively. The blue color represents the regular regions, while the remaining domain is responsible for the system's chaotic motion. These two diagrams mostly coincide, which confirms the hyperchaotic nature of the system

under the initial condition

$$\ell(0) = 3, \quad \varphi_1(0) = 0, \quad \varphi_2(0) = \frac{\pi}{4}, \quad v(0) = \omega_1(0) = \omega_2(0) = 0. \quad (3.2)$$

As the considered system has a six-dimensional phase space, there are six Lyapunov exponents $\Lambda = \{\lambda_i\}$, $i = 1, \dots, 6$, where λ_1 is the largest Lyapunov exponent. As we can notice, the integration time 5000 units was sufficient to ensure the convergence of the Lyapunov exponents. Moreover, we observe that they appear in additive inverse pairs, so they sum to zero. This is by Liouville's theorem [100], which states that a conservative Hamiltonian system is volume-preserving. Therefore, if λ is a Lyapunov exponent, then $-\lambda$ is also. Due to the existence of the first integral in the system (2.6), which is the conservation of total energy E , two Lyapunov exponents tend to zero. The numerically computed values of λ_3, λ_4 are not exactly zero on finite time scales. Therefore, for practical purposes of our investigation, we take the zero value of the Lyapunov exponent whenever it is less than 0.003. Thus, the possible Lyapunov exponent spectrum of the system (2.6) is $\Lambda = \{\lambda_1, \lambda_2, 0, 0, -\lambda_2, -\lambda_1\}$, where λ_1 is the maximum Lyapunov exponent. As λ_1 and λ_2 are non-zero for the given values of the parameters (3.1) and the initial conditions (3.2), the system dynamics is hyperchaotic.

By repeating the above procedure with varying parameter values or initial conditions, we can create Lyapunov diagrams on the parameter plane. Figs. 3-4 present diagrams of Lyapunov exponents λ_1 and λ_2 for the parameters pairs (μ, δ) with varying values of ω . Color scales are proportional to the magnitudes of the exponents λ_1 and λ_2 , respectively. The colorful diagrams were obtained by numerical computations of Lyapunov exponents on a grid of 400×400 values of parameters $\mu, \delta \in [0.1, 4]$ with initial conditions (3.2). These diagrams show how changes in the values of the parameters (μ, δ) affect the dynamics of the system. The blue region corresponds to regular, non-chaotic oscillations, and the rest of the domain is responsible for the chaotic motion with two positive Lyapunov exponents. As we can see in Fig. 3, for $\omega = 1$ the diagrams of exponents λ_1 and λ_2 mostly coincide confirming the hyperchaotic nature of the system. For relatively small values of the mass ratio $\mu \in [0.1, 0.75]$ and for highly stretched $\delta \in [0.1, 0.5]$, and compressed $\delta \in [3.5, 4]$ spring, the strength of chaos is prominent with the largest Lyapunov exponent reaching its maximal value $\lambda_1 \approx 0.19$. In the prescribed Lyapunov diagram, we can see that there are four large regular seas separated by chaotic regions. Inside these regular regions, one can find values of μ and δ for which the system's motion is periodic. We will explore this in more detail in the next subsection.

The situation is completely different when we set $\omega = 0$. The diagram illustrated in Fig. 4 shows complex dynamics for a wide range of values (μ, δ) , while the diagram of λ_2 presents a regular pattern with $\lambda_2 \approx 0$ for every (μ, δ) . It is caused by the presence of the additional first integral inside the system. Indeed, for $\omega = 0$ the

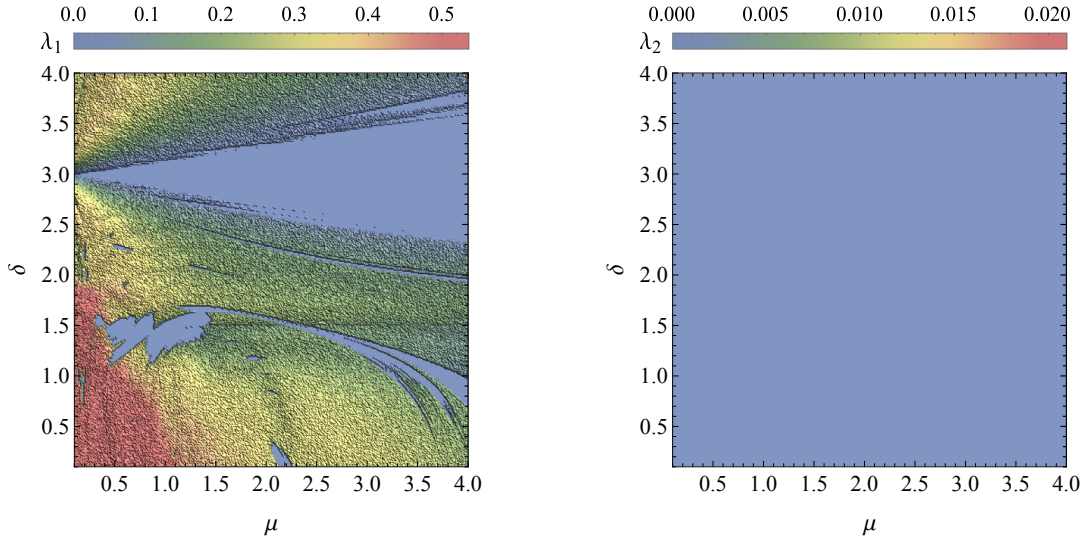


Figure 4: (Color online) The diagrams of two Lyapunov exponents λ_1 and λ_2 computed for the grid of 400×400 values of $\mu, \delta \in [0.1, 4]$ with $\omega = 0$. The numerical integrations were carried out successively for the initial condition (3.2). The color scales are determined by the magnitudes of λ_1 and λ_2 , respectively. Blue regions correspond to regular (non-chaotic) dynamics, while the remaining domain is responsible for complex dynamics. Due to the presence of the additional first integral, the exponent $\lambda_2 = 0$

system possesses symmetry \mathbb{S}^1 since Lagrangian (2.5) depends only on angle differences. Therefore, for $\omega = 0$ the system can be reduced to a model of two degrees of freedom for which the Poincaré sections method can be adopted. The above makes the Lyapunov exponents spectrum a possible indicator for searching for additional first integrals and integrable dynamics. Indeed, in a recent paper [24], the author algorithmically used the method of Lyapunov exponents in the systematic search for the first integrals of the systems. When examining the bottom left diagram presented in Fig. 4, we can observe some kind of tunnel that leads to the regular sea through a chaotic area. As we shall discover, many periodic solutions exist within this region.

Lyapunov exponent diagrams can also be useful for understanding system dynamics and the strength of chaos by plotting the values of the largest Lyapunov exponent λ_1 as a function of initial conditions of state variables. Therefore, a qualitative and quantitative description of chaos is possible. For our purpose, it is sufficient to plot the largest Lyapunov exponent to distinguish the regions with chaotic motion from the regular ones. In Fig. 5, we present the polar plots of Lyapunov exponents diagrams for fixed values of the parameters

$$\mu = 3, \quad \delta = 1, \quad \text{with } \omega \in \{1, 1.6, 6, 100\}, \quad (3.3)$$

and initial conditions were chosen as

$$\ell(0) \in [0.001, 5], \quad \varphi_1(0) = 0, \quad \varphi_2(0) \in [-\pi, \pi], \quad v(0) = \omega_1(0) = \omega_2(0) = 0. \quad (3.4)$$

Here, $\ell(0)$ and $\varphi_2(0)$ are treated as the control parameters. The colorful diagrams visible in Fig. 5 were obtained by numerically computing Lyapunov's exponents on a grid of 400×400 values of $(\ell(0), \varphi_2(0))$ and then plotted in the polar-plane. Therefore, in the radial direction, we measure the ratio of the initial lengths of the pendulums, that is, $\ell(0)$, while in the angular direction values of $\varphi_2(0)$ are given. The color scale is proportional to the magnitudes of the largest Lyapunov exponent λ_1 .

The diagrams presented in Fig. 5 are very useful because they give information on how the change in the initial length of the spring $\ell(0)$ and the initial swing angle $\varphi_2(0)$ affect the dynamics of the whole system. Moreover, we can easily estimate the range of initial conditions for which the motion of the system is regular. For example, for $\omega = 1$, which indicates $gl_1 = k/m_2$, the amount of area responsible for the chaotic motion of the system is prominent. For the initial values $\ell(0) \in (0, 1)$, so the spring is highly compressed, the system performs complex dynamics for arbitrary values of $\varphi_2(0) \neq 0$. However, for $\ell(0) \in (1, 3)$ and for sufficiently small amplitudes of $\varphi_2(0) \in (-0.4\pi, 0.4\pi)$, the system performs regular, non-chaotic oscillations. On the other hand, for larger values of $\varphi_2(0)$, the chaotic motion occurs and has maximum strength around $\varphi_2(0) \approx \pm\pi$, as expected. For larger values of $\ell(0)$, so the spring is initially stretched, the motion of the system is highly complex even

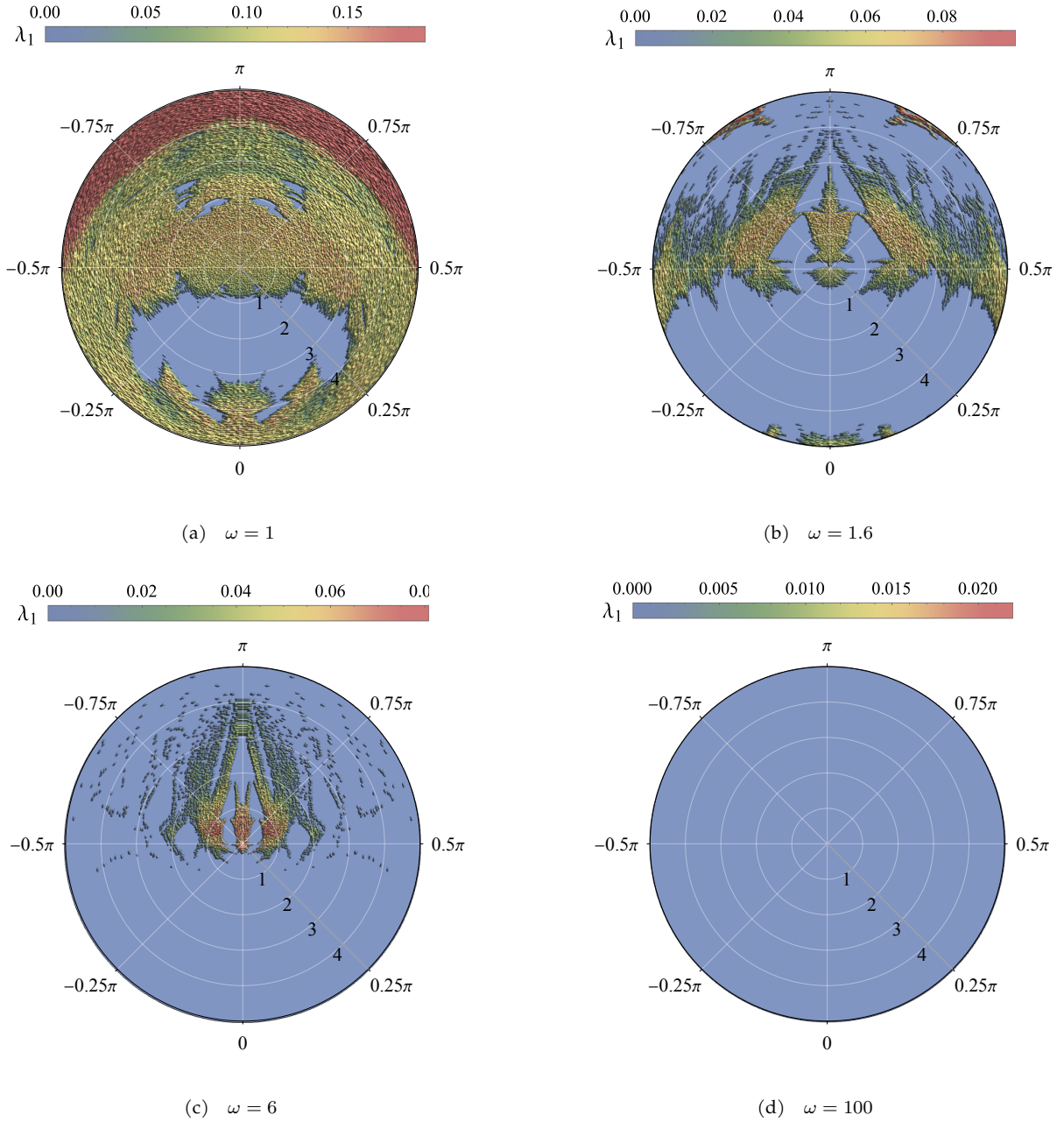


Figure 5: (Color online) The Lyapunov diagrams for the system (2.6) in the polar plane $(\ell(0), \varphi_2(0))$ constructed for the parameters $\mu = 3, \delta = 1$ with varying ω , and initial conditions (3.4). In the radial direction, we measure $\ell(0) \in [0.001, 5]$; in angular direction, we measure $\varphi_2(0) \in [-\pi, \pi]$. The color scale is proportional to the magnitude of the largest exponent λ_1 . The plots visualize two zones: regular and chaotic. Blue regions indicate regular dynamics, while regions with $\lambda_1 > 0$ correspond to the system's chaotic behavior

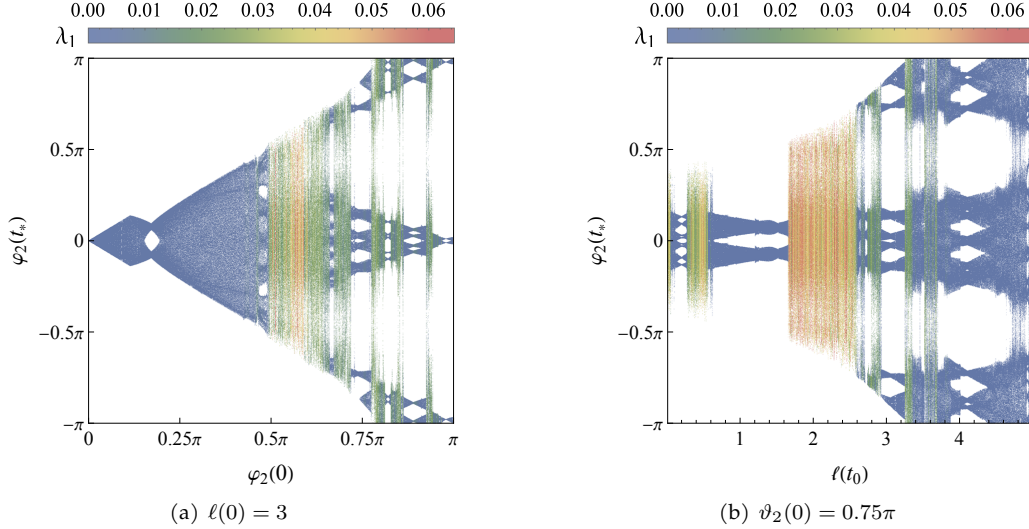


Figure 6: (Color online) Phase-parametric diagrams of system (2.6) versus: a) the initial swing angle $\varphi_2(0) \in [0, \pi]$, b) the ratio of the initial lengths of the pendulums $\ell(0) \in [0.001, 5]$. The initial conditions and values of the parameters are taken from Fig. 5(b). There are two cases to consider: a) we move in the angular direction of the Lyapunov diagram 5(b) for $\ell(0) = 3$ and $\varphi_2(0) \in [0, \pi]$; b) we choose the initial swing angle to be $\varphi_2(0) = 0.75\pi$ and move in the radial direction of the Lyapunov diagram 5(b) for $\ell(0) \in [0.001, 5]$. Here $\varphi_2(t_*)$ are the values of φ_2 , when the trajectory crosses the section plane $\ell = 2.6$, for some t_* . The diagram is combined with the largest Lyapunov exponent λ_1 and the color scale is proportional to its magnitude. Very good agreement of the phase-parametric diagram with the Lyapunov diagram 5(b) is observed. The coexistence of periodic, quasi-periodic, and chaotic orbits together with „periodic windows“ between chaotic layers is visible. Exemplary periodic, quasi-periodic, and chaotic orbits are plotted in Fig. 7

for very small initial amplitudes of φ_2 . The rest of the Lyapunov diagrams visible in Fig. 5, show the relation between initial values of $(\ell(0), \varphi_2(0))$ and further increasing values of ω . We see that for higher values of ω , the system is less chaotic since λ_1 is decreasing. Moreover, the growth of areas responsible for the regular oscillations is visible. In particular, for $\omega = 100$, there are no signs of chaos since $\lambda_1 \approx 0$, for every initial condition. The above suggests the integrability of the system for $\omega \rightarrow \infty$. This particular case will be examined in more detail in Section 3.3.

3.2. Bifurcation diagrams and Lyapunov exponents

The Lyapunov exponents is the essential tool for giving the quantitative description of chaos. However, in the context of the Hamiltonian system, this method has one weak point. Namely, in the blue regions of the Lyapunov diagrams as in Fig. 3-5, where $\lambda_1 \approx 0$, we are unable to distinguish values of the control parameters, for which the motion of the system is periodic or quasi-periodic. This lack of distinction is a significant inconvenience since knowledge about the existence of resonance orbits in Hamiltonian dynamical systems is crucial. Nevertheless, constructing phase-parametric diagrams is an effective way to solve this problem.

The phase-parametric diagram gives a qualitative description of the system dynamics by plotting a state variable as a function of a suitably chosen control parameter [23, 24]. However, in the context of Hamiltonian systems, it is convenient to show intersections of phase curves with a properly chosen surface of section. In this way, periodic, quasiperiodic, and chaotic orbits are distinguishable. As the treated system is a spring-pendulum system, we use initial $\varphi_2(0)$ and $\ell(0)$ as bifurcation parameters. As the cross-section plane, we chose the length of the spring-mass at the equilibrium, that is, $\ell = \delta + \omega$.

Fig. 6 presents the phase-parametric diagrams of the system computed for two one-parameter families of initial conditions $(\ell(0), \varphi_2(0))$ taken from Fig. 5(b). In Fig. 6(a), we move in the angular direction of the Lyapunov diagram 5(b) with $\ell(0) = 3$ and $\varphi_2 \in [0, \pi]$, while Fig. 6(b) corresponds to the case that we chose $\varphi_2(0) = 0.75\pi$ and we move in the radial direction of the Lyapunov diagram 5(b) with $\ell(0) \in [0.001, 5]$. That is, for a given initial condition, we numerically integrate the equations of motion (2.6) and build the diagram by collecting points $\varphi_2(t_*)$ when $\ell(t) = 2.6$, with varying values of initial $\varphi_2(0)$ and $\ell(0)$. Furthermore, to make the analysis more effective, we joined the phase-parametric diagrams with Lyapunov exponents computed previously in Fig. 5(b). The color scale is proportional to the magnitude of λ_1 . At first, we observe an excellent

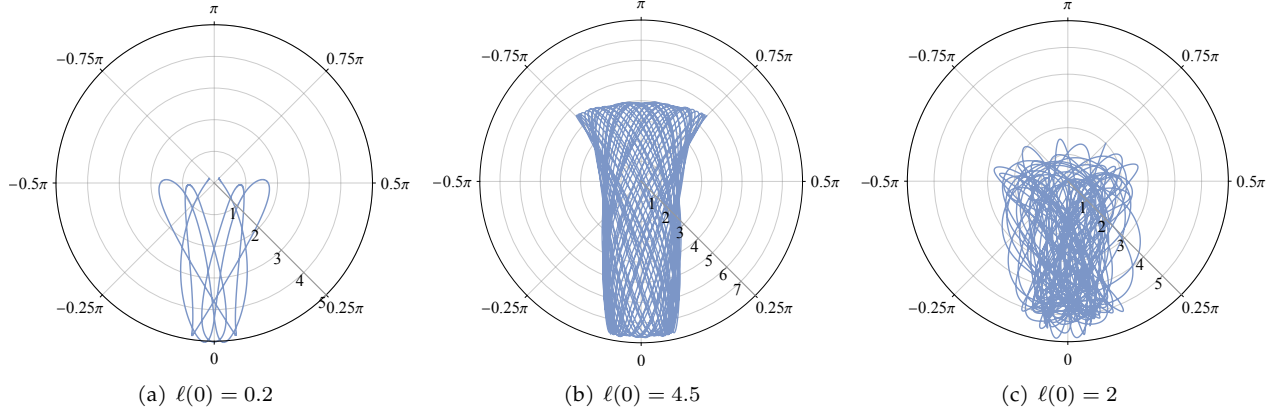


Figure 7: (Color online) Polar plots of exemplary a) periodic, b) quasi-periodic, and c) chaotic orbits of the double spring pendulum. The parameters values and initial conditions were taken from the phase-parametric diagram presented in Fig. 6(b). In the radial direction, we measure $\ell(t)$; in the angular direction, we measure $\varphi_2(t)$

correspondence of the phase-parametric diagram with λ_1 . The blue regions with $\lambda_1 \approx 0$ correspond to regular oscillations, while other areas are responsible for the chaotic behavior of the system. Moreover, while not visible via Lyapunov exponents diagrams, from the regular regimes, we can distinguish periodic orbits from quasi-periodic ones. Fig. 6(a) starts with a regular regime corresponding to periodic and quasi-periodic oscillations of the spring near the equilibrium. Further increasing values of the initial swing angle φ_2 indicate that the regular pattern divergences and in the neighborhood of the point $\varphi_2(0) = \pi/2$ the motion becomes chaotic with non-zero values of λ_1 . However, even for very high values of $\varphi_2(0)$, we can still find periodic solutions located in the small gaps between completely chaotic regions. Fig. 6(b) presents a quite different picture. The phase parametric diagram indicates the chaotic motion of the system for a very small initial length of the spring $\ell(0) \in [0.001, 0.1]$. This was quite expected because the natural length of the spring is $\delta = 1$. Therefore, for the initial length $\ell(0) \in [0.001, 0.1]$, the spring is highly compressed. Surprisingly moving further to the right, in the neighborhood of the point $\ell(0) = 0.2$, the periodic solution appears. However, we claim that this periodic solution is unstable because, in the right neighborhood of this, we observe the rise of chaotic behavior of the system over the regime $\ell(0) \in [0.3, 0.63]$. For higher values of the control parameter $\ell(0)$, the motion is regular up to the point $\ell(0) \approx 1.7$, where the hyperchaos takes place in the wide range of $\ell(0) \in [1.7, 2.65]$. In addition, regular and chaotic regions coexist; As the initial length $\ell(0)$ increases, the appearance of periodic windows between chaotic layers is visible. For better understanding, in Fig. 7 polar plots of exemplary nonsingular orbits of the system with different initial conditions are taken from the phase-parametric diagram illustrated in Fig. 6(b).

As we have already seen, the Lyapunov exponents is an essential tool for giving a qualitative description of chaos. We used this method to specify areas on the two-parameter diagrams for which motion of the system is regular or chaotic. On the other hand, computations of phase-parametric diagram are effective in finding periodic orbits and their number or presenting the routes to the chaos of a given dynamical system. Therefore, it is reasonable to combine these two methods more systematically. Let us show this in the example of parameters corresponding to the Lyapunov diagram 5(b). First, we select from the diagram these pairs of $(\ell(0), \varphi_2(0))$, such that $\lambda_1 = 0$. Hence, we obtain a grid of n initial conditions for which the motion of the system is non-chaotic. Next, for each element of the grid, we compute the phase parametric diagram by collecting points $\varphi_2(t_*)$ periodically, when $\ell(t_*) = \delta + \omega = 2.6$ for a wide range of t . As a result, we obtain n lists of points $\varphi_2(t_*)$. Then, in each list, we look for a scheme of repeating values of $\varphi_2(t_*)$ in a certain order. The above can be effectively handled with the help of Mathematica. In this way, the rough distinction between periodic solutions from quasi-periodic ones is possible. The result is presented in Fig. 8, where the periodic points are depicted in the Lyapunov diagram 5(b). Now, we have the complete picture of the system dynamics by specifying intervals where the motion is chaotic, quasi-periodic, or periodic. In fact, each white point corresponds to different initial conditions $(\ell(0), \varphi_2(0))$ for which the spring pendulum motion is periodic with certain frequency ratios. In Fig. 9, we show the polar graphs showcasing exemplary periodic orbits of the system.

In Fig. 10, we present the Lyapunov diagrams previously shown in Figs. 3-4, depicting periodic points. Specifically, these diagrams illustrate the values of the parameters (δ, μ) for which the system, under the initial

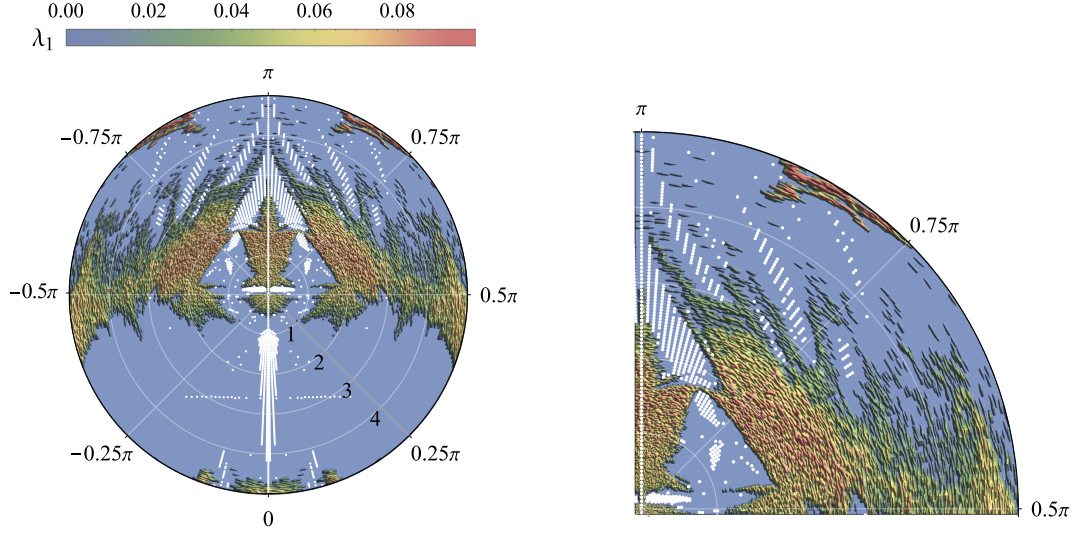


Figure 8: (Color online) The Lyapunov diagram visible in Fig. 5(b) with depicted periodic orbits. Each white point corresponds to distinct initial conditions $(\ell(0), \varphi_2(0))$ for which the motion of the spring pendulum is periodic with certain ratios of frequencies. The polar plots of exemplary periodic orbits are depicted in Fig. 9

condition (3.2), moves periodically with certain frequency ratios. In Fig. 10(a), a large cluster of periodic solutions can be observed in the left center of the diagram, along with several scattered periodic solutions throughout. The polar plots of periodic orbits for given values of the parameters (μ, δ) are depicted in Fig. 11. Fig. 10(b) exhibits a different pattern, where instead of one cluster of periodic solutions, we observe a myriad of periodic solutions forming resonance-like curves. The crosses in the diagram at $\delta = 3$ represent the equilibrium points of the system. The abundance of periodic solutions can be attributed to the fact that, for $\omega = 0$, the system is a two-degree-of-freedom model, which simplifies its complexity. Fig. 12 presents polar plots of exemplary periodic orbits for prescribed values of the parameters (μ, δ) .

3.3. Poincaré cross-sections and Lyapunov exponents

As evidenced in Fig. 4, for $\omega = 0$, one additional Lyapunov exponent is zero for arbitrary values of the remaining parameters (δ, μ) . This occurs because, for $\omega = 0$, there exists an additional first integral

$$F = \partial_{\omega_1} L + \partial_{\omega_2} L = \text{const}. \quad (3.5)$$

Hence, the total angular momentum of the pendulums with respect to the suspension point is the conserved quantity. Therefore, it is reasonable to introduce new variables defined by

$$\begin{aligned} \varphi(t) &= \varphi_1(t), & \vartheta(t) &= \varphi_1(t) - \varphi_2(t), \\ \omega(t) &= \omega_1(t), & \Omega(t) &= \omega_1(t) - \omega_2(t). \end{aligned} \quad (3.6)$$

At the level $F = c$, the system reduces to a system of two degrees of freedom with the following Lagrange function

$$\begin{aligned} L &= T - V_{\text{eff}}, \\ T &= \frac{1}{2} \left(1 - \frac{\sin^2 \vartheta}{1 + \mu + 2\ell \cos \vartheta + \ell^2} \right) v^2 + \frac{1}{2} \left(\frac{\mu + \sin^2 \vartheta}{1 + \mu + 2\ell \cos \vartheta + \ell^2} \right) \ell^2 \Omega^2 - \left(\frac{(\cos \vartheta + \ell)\ell \sin \vartheta}{1 + \mu + 2\ell \cos \vartheta + \ell^2} \right) v\Omega, \\ V_{\text{eff}} &= \frac{c^2}{2(1 + \mu + 2\cos \vartheta + \ell^2)} + \frac{1}{2} (\delta - \ell)^2. \end{aligned} \quad (3.7)$$

As the motion of the reduced system takes place in four-dimensional phase space, we can effectively compute the Poincaré cross-sections. The main idea of the Poincaré cross sections is very simple. We consider a surface

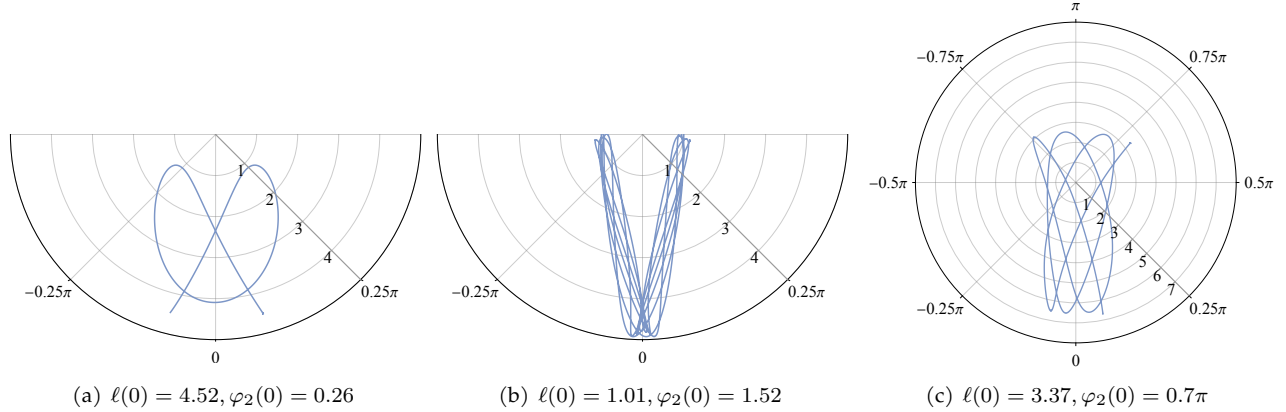


Figure 9: (Color online) Polar plots of exemplary periodic orbits of the double spring pendulum. In the radial direction, we measure $\ell(t)$; in the angular direction, we measure $\varphi_2(t)$. Each set of initial conditions $(\ell(0), \varphi_2(0))$ corresponds to a specific white dot marked on the Lyapunov diagram presented in Fig. 8

(in our case $\ell_0 = 1$) in the phase space that is traversed by all trajectories. Together with the energy conservation $E = T + V_{\text{eff}}$, we have a two-dimensional surface embedded in the (ϑ, Ω, v) -space. This surface is formed by two connected components $v_{\pm} = v_{\pm}(E, \vartheta, \Omega)$, which are two roots of the quadratic equation for v imposed by energy conservation $E = \text{const}$. For convenience, we choose $v > 0$, and as the coordinates on this surface, we take (ϑ, Ω) . As a result, we obtain a pattern in the plane, which can be easily visualized and interpreted. If the motion of the system is periodic, the trajectory passes through the plane only in a finite number of intersections. The quasi-periodic motion is manifested by continuous loops on the section plane, while a chaotic trajectory intersects the section plane in scattered, random-looking points.

Fig. 13 shows six Poincaré sections and their corresponding two-parameter Lyapunov diagrams of system (3.7). These were constructed with gradually increasing values of the energy E , for the following constant parameters

$$\mu = 3, \quad \delta = 1, \quad c = 0. \quad (3.8)$$

It is easy to verify that the minimum energy of the system (3.7), corresponding to the equilibrium position of the pendulums when $\ell_0 = 1$ is equal to $E_0 = 0$. Therefore, we may expect regular behaviors of the system for energies close to E_0 . The Poincaré section visible in Fig. 13(a) confirms our suspicion. At the energy level $E = 0.001$ it presents a very regular image. We observe three particular periodic solutions located at $\vartheta = 0, \pm\pi$ with $\Omega = 0$, surrounded by invariant tori. Each closed loop corresponds to a quasi-periodic motion. These three particular solutions are visible in the remaining Poincaré sections depicted in Fig. 13(b-c) as well. This is because the equations of motion governed by Lagrange function (3.7) have an invariant manifold $\mathcal{M} = \{(\ell, v_\ell, \vartheta, \Omega) \in \mathbb{R}^4 \mid \vartheta = \Omega = 0\}$. The Lagrange function (3.7) constrained to \mathcal{M} , reduces to a system of one degree of freedom that defines the harmonic oscillator with solutions $\ell(t) = \ell_0 + \sqrt{2E} \cos t$, and $v = \dot{\ell}(t)$ with $\vartheta(t) = \Omega(t) = 0$. We may conclude that for such a small energy value the motion of the system is almost integrable. However, what is not visible in the Poincaré plane, the corresponding Lyapunov diagram indicates that the curve, which separates librational motion from the rotational one, is indeed, weakly" chaotic. So, we claim that this curve is a source of the chaotic motion of the system since $\lambda_1 > 0$.

The situation becomes more complex when we increase the energy to the value $E = 0.017$. Fig. 13(b) confirms the chaotic nature of the reduced system. Most of the invariant tori, responsible for the rotational motion of the system, decay giving rise to periodic orbits bounded by chaotic remains of the separatrices. Indeed, the corresponding Lyapunov diagram shows a variety of decayed separatrices. This is one of the main benefits of combining Poincaré cross sections with Lyapunov diagrams. For large values of initial conditions (in our cases 500×500) uniformly distributed in the available area of the Poincaré plane, with the help of Lyapunov exponents, we can detect „chaotic folds" responsible for weak chaotic motion. Thus, the Lyapunov exponents diagram serves as a complementary tool to the Poincaré sections, providing insights into chaotic dynamics that may not be apparent from the latter, which can be constructed for a much smaller grid of initial conditions from visual reasons. Fig. 13(c) shows the Poincaré section and the Lyapunov diagram constructed for $E = 0.05$. As

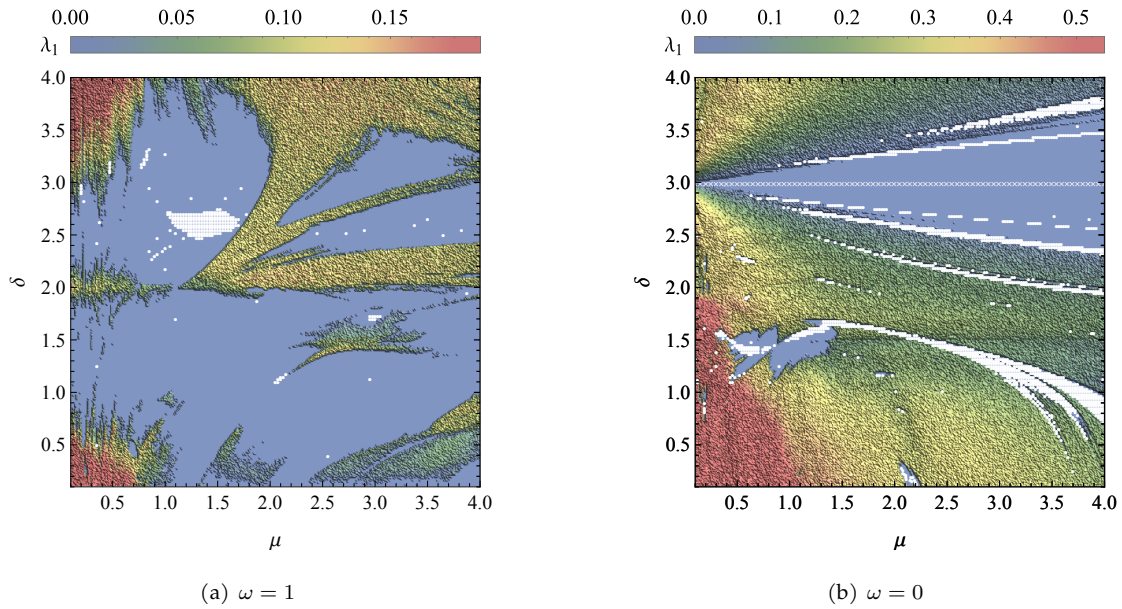


Figure 10: (Color online) The Lyapunov diagrams presented in Figs. 3-4 with depicted points corresponding to values of the parameters (δ, μ) for which motion of the spring pendulum is periodic with certain ratios of frequencies. The polar plots of exemplary periodic orbits are shown in Figs. 11-12

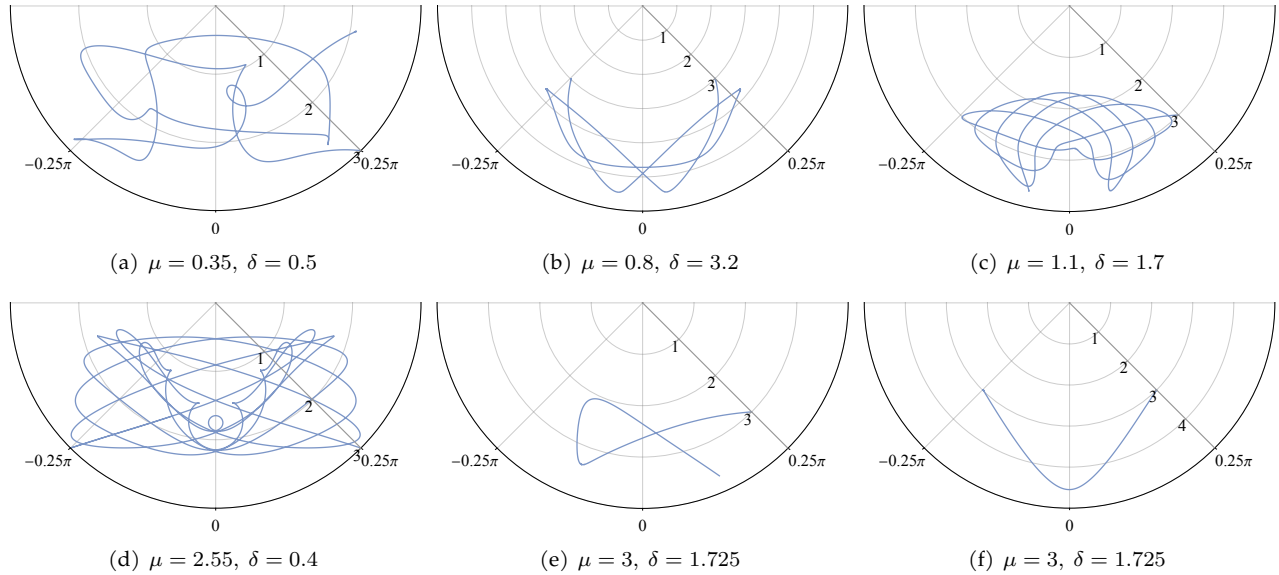


Figure 11: (Color online) Polar plots of exemplary periodic orbits of the double spring pendulum. The parameters values (μ, δ) and initial conditions were taken from the Lyapunov diagram presented in Fig. 10(a). In the radial direction, we measure $\ell(t)$; in the angular direction, we measure $\varphi_2(t)$

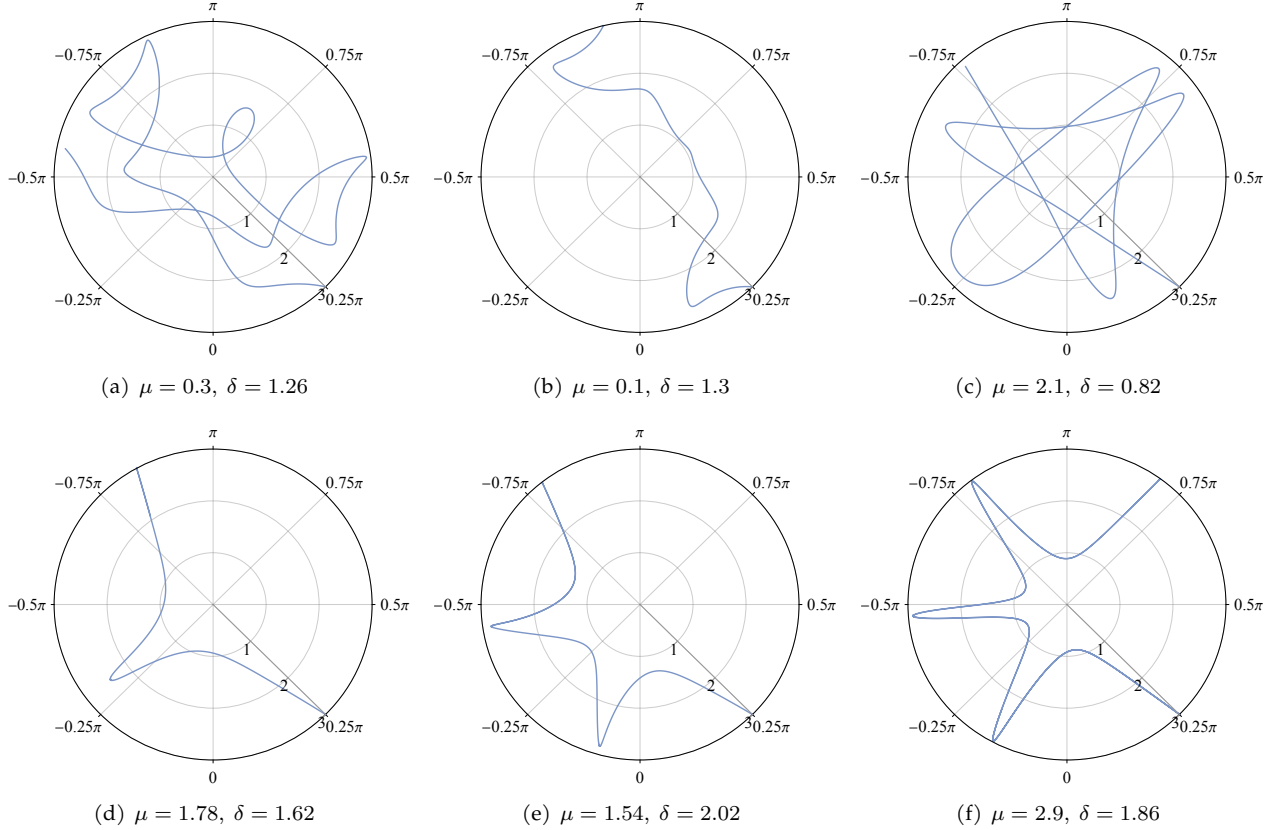
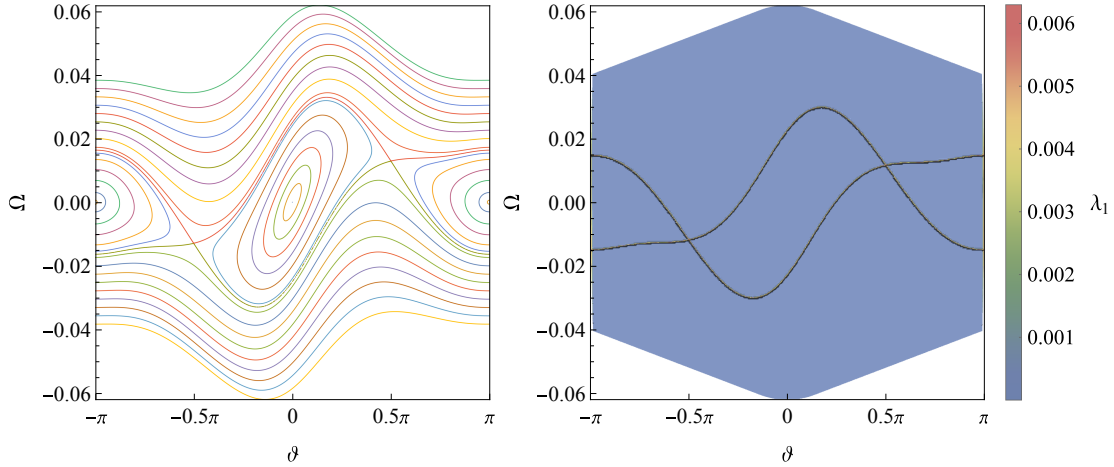


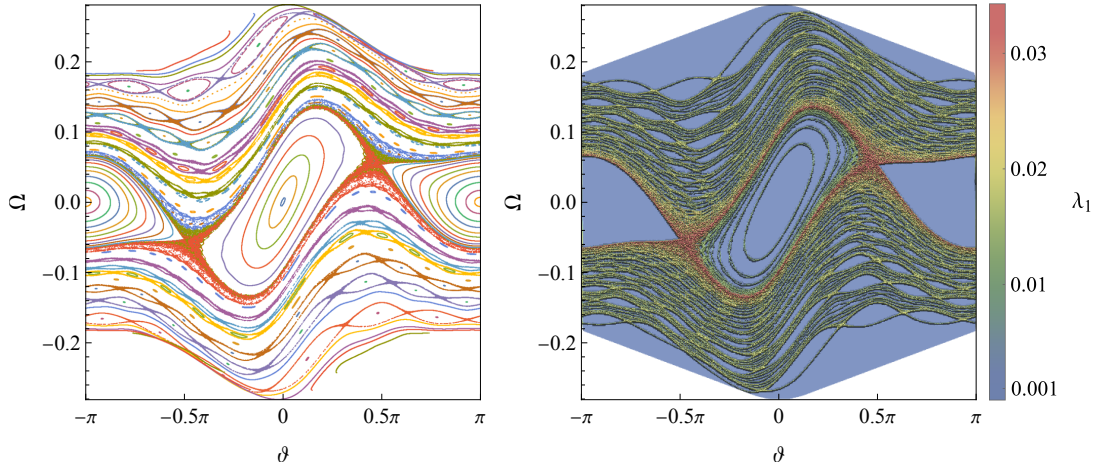
Figure 12: (Color online) Polar plots of exemplary periodic orbits of the double spring pendulum. The parameters values (μ, δ) and initial conditions were taken from the Lyapunov diagram presented in Fig. 10(b). In the radial direction, we measure $\ell(t)$; in the angular direction, we measure $\varphi_2(t)$

the energy value is increased, the area at the Poincaré plane responsible for the chaotic motion of the system also increases, as expected. These random-looking points correspond to the fact that trajectories can freely wander over large regions of the phase space. The trajectories are no longer confined to the surfaces of nested tori in contrast to the integrable system. The tori are destroyed and the trajectories begin to move outside them. The corresponding Lyapunov diagram finally confirms that for the prescribed values of the parameters the reduced system governed by Lagrange function (3.7) is highly not integrable Hamiltonian system.

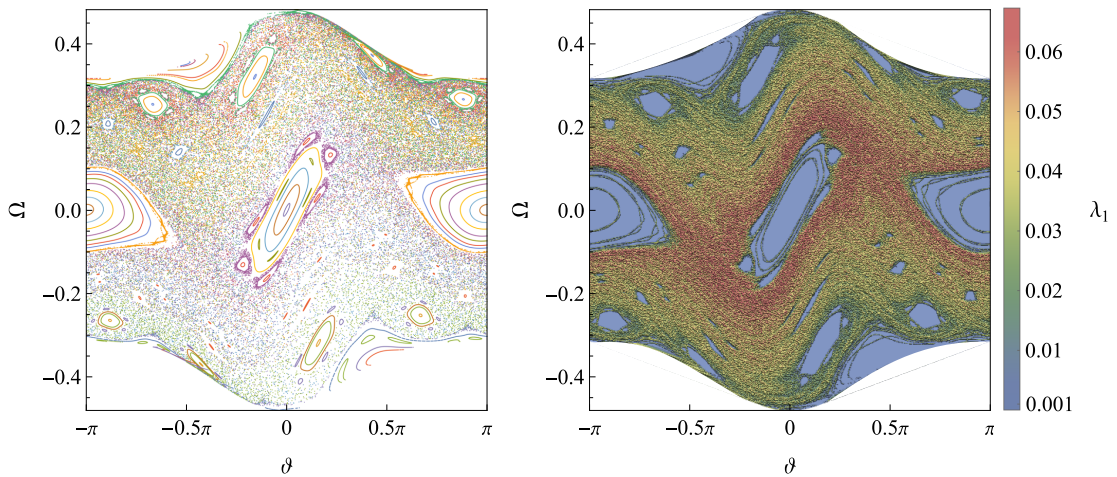
With the help of Lyapunov exponents, we can easily estimate the percentage of chaos equipped in the available area of the Poincaré plane as a function of the energy. Indeed, for a large number of initial conditions uniformly distributed in the available area of the Poincaré plane determined by the energy value, we compute repeatedly the largest Lyapunov exponents. Next, we calculate the ratio of the number of points with a Lyapunov exponent different from zero (in practice larger than 0.003) to the total amount of initial conditions. Likewise, we can calculate the maximum and mean values of the Lyapunov exponent for a given energy. Results for $E \in [0, 0.2]$ are shown in Fig. 14. As expected, for values of the energy close to the energy minimum $E_0 = 0$, the percentage of chaos is almost zero. This is in accordance with the Poincaré section visible in Fig. 13(a), where the weak chaos appears only in the area where the separatrix was located. Next, we have the classical transition from a regular regime at low energies to a highly chaotic regime at larger ones. Indeed, the percentage of chaos increases rapidly, and at $E = 0.05$ it covers 75% of the available area of the Poincaré section plane visible in Fig. 13(c). Then, for larger values of the energy, the system monotonically goes to an almost fully ergodic one with the percentage of chaos very close to 95%. The maximal and average values of λ_1 show a similar behavior starting from zero value at the energy minimum and then increasing linearly up to their highest values reached at $E = 0.2$. As we have seen, the Poincaré cross-section method is an effective tool for giving a quick insight into the dynamics of the considered model. Indeed, Fig. 13(b) shows the beautiful co-existence of periodic, quasi-periodic, and chaotic motion. To show the detailed structure of this co-existence, we have to



(a) Energy $E = E_0 + 0.001$, Regular domain with the chaotic remains of a separatrix



(b) Energy $E = E_0 + 0.017$, the beauty of the coexistence of periodic, quasi-periodic, and chaotic orbits



(c) Energy $E = E_0 + 0.05$, the highly chaotic stage system's dynamics

Figure 13: (Color online) The Poincaré sections of the system (3.7) and their corresponding Lyapunov diagrams, constructed for constant values of the parameters $\mu = 3$, $\delta = 1$, and $c = 0$ with a gradually increasing energy level E , where E_0 is the energy minimum. The cross-section plane was defined as $\ell = 1$ with the direction $v > 0$. In the Poincaré sections, the colors are associated with different classical trajectories. For the Lyapunov exponents, the color code is given on the bar. Blue regions indicate regular dynamics, while regions with $\lambda_1 > 0$ correspond to the system's chaotic behavior

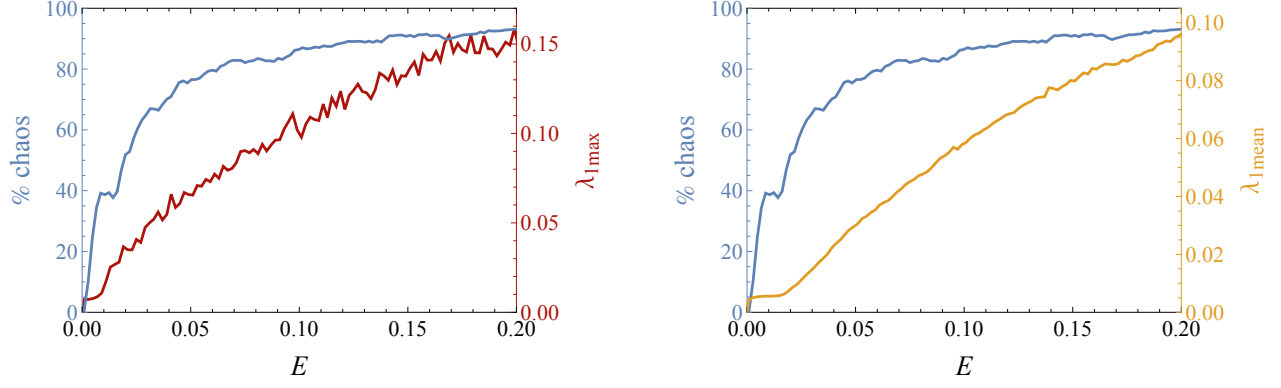


Figure 14: (Color online) The percentage of chaos against the maximal and mean values of the largest Lyapunov exponent λ_1 in phase space as a function of the energy

increase the number of initial conditions and perform successive magnifications of the cross-section. However, for a large number of initial conditions, in the global cross-section, certain characteristic patterns are not visible. In Fig. 15(a), we present the Poincaré sections constructed for $3 \cdot 10^3$ initial conditions uniformly distributed in the available area of the Poincaré plane. As we can see, it is hard to distinguish in the global view periodic orbits from quasi-periodic and chaotic ones because the orbits are located very close to each other. Since Poincaré it is known that periodic solutions of the considered system form the skeleton of the structure of the phase space. Of course, there are many approaches for finding and studying periodic solutions; for instance, see the newest one [101]. Here, we propose to locate stable periodic solutions in the global cross-section and use them as a kind of filter.

To find periodic orbits and their numbers in the available area of the Poincaré plane, we can use the analogous approach as in Section 3.2. We make the following. We fix the value of the energy first integral E . Then, for a set B containing a large number of initial conditions uniformly distributed in the available area of the Poincaré plane, we compute the largest Lyapunov exponent λ_1 . Elements in B with $\lambda_1 > 0$ are disregarded. In this way, we obtain a subset of n initial conditions for which the motion of the system is non-chaotic. Next, for each initial condition, we compute the Poincaré cross sections with a sufficiently large number of sections restricted to the plane (ϑ, Ω) . As a result, we obtain n lists with section points (ϑ, Ω) . Then, we perform a similarity check. Namely, in each list, we look for the scheme of repeated values of (ϑ, Ω) in a certain order. If the motion is periodic, then we have a finite number of repeating points. The quasi-periodic motion is manifested by the infinite number of distinct points. In this way, the rough but effective distinction between periodic and quasi-periodic orbits is possible. The results of exemplary computations for $E = 0.017$ are presented in Fig. 15(b). It is the Poincaré section plane, similar to the one shown in Fig. 13(b), but constructed for $3 \cdot 10^4$ initial conditions, where chaotic and quasi-periodic trajectories are eliminated, leaving only solutions close to stable periodic orbits. This plot, which we call the filtered Poincaré cross section, shows the rich structure of the system dynamics which is hidden in a usual cross-section. We get a vast number of periodic orbits of various ratios of frequencies, even the ones corresponding to high-order resonances. This leads to the fact that the invariant tori, which are located near these high-order resonance orbits, are prone to decay with further increasing energy. This is visible in Fig. 13(c), where most of the tori decay into global chaos.

Repeating the above computations for a certain range of energy, we can estimate the number of stable periodic solutions as a function of the energy. In Fig. 16, we can see a representation of the relationship between the percentage of chaos and the number of stable periodic orbits available in the phase space. The left axis shows the percentage of chaos, while the right axis displays stable periodic orbits as a function of energy E . When the energy is close to the energy minimum, the percentage of chaos is almost zero, and we have several periodic orbits. However, for slightly larger values of the energy, the invariant tori broke up giving rise to periodic solutions. We observe that the number of periodic orbits and the percentage of chaos increase rapidly as energy increases as well. At the energy level $E = 0.017$, the number of distinct periodic orbits is maximal with $N = 331$, while the chaos occupies 40% of the available area of the Poincaré plane, see the corresponding Poincaré sections illustrated in Figs. 13 and 15. As the energy increases, the periodic orbits successively diverge into global chaos, making the available phase space almost fully ergodic.

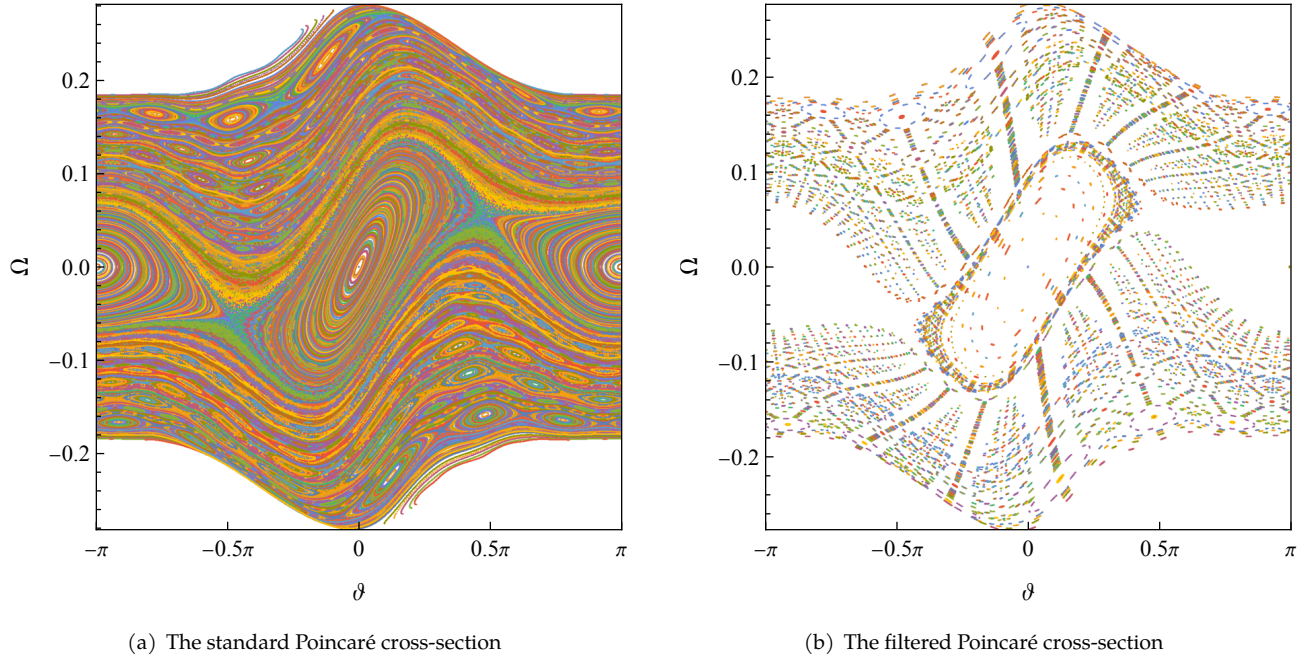


Figure 15: (Color online) The Poincaré sections of the system (3.7) constructed for: a) $3 \cdot 10^3$ and b) $3 \cdot 10^4$ initial conditions uniformly distributed at the available area. The parameters were chosen by $\mu = 3, \delta = 1, c = 0$, and the cross-section plane was defined as $\ell = 1$ with the direction $v > 0$. The left picture is unclear since periodic, quasi-periodic, and chaotic orbits overlap. The right Poincaré section is filtered from chaotic and quasi-periodic orbits, presenting the skeleton structure of stable periodic solutions only

Up to now, we have examined the behavior of the model by using Poincaré sections while altering the system's energy. However, it would be worthwhile to conduct a similar analysis keeping the energy constant and gradually increasing the mass ratio μ . In Figs. 17-18, we present four pairs of Poincaré sections and corresponding Lyapunov diagrams created for $\omega = \delta = 1$ with varying values of μ at a constant energy level $E = E_0 + 0.5$, where $E_0 = 0$ represents the minimum energy at rest. As we can notice, for the relatively high value of the energy level, the values of ϑ span the whole range $\vartheta \in [-\pi, \pi]$ and the angular velocity Ω reaches high values in comparison to Fig. 13. For the mass ratio $\mu = 5$, the system reveals highly chaotic dynamics visible in terms of scattered points at the Poincaré section plane. Indeed, almost all invariant tori decay into the global chaos and the maximal Lyapunov exponent reaches $\lambda_1 \approx 0.086$. The situation changes when we increase the value of μ , for instance, up to $\mu = 10$. At the corners of the plane, illustrated in Fig. 17(b), we observe the emergence of four stable periodic solutions bounded by quasi-periodic loops. In the central region, a striking coexistence of periodic and chaotic chains becomes apparent. This is particularly evident in the associated Lyapunov diagram, where each chaotic fold is identified. As we increase the mass ratio up to $\mu = 15$, the dynamics of the system become less chaotic which is clearly visible in Fig. 18(a). The region responsible for chaotic motion at the Poincaré plane also decreases with decreasing values of λ_1 . This trend becomes even clearer when we further increase the mass ratio up to $\mu = 50$. As we can notice, even for such a high value of energy, the dynamics of the system is very regular. In the Poincaré section plane, illustrated in Fig. 18(b), we can observe the shapely elegant invariant tori suggesting the system's integrability. There are no signs of chaotic motion at all. Instead of that, we can detect two stable particular periodic solutions enclosed by the separatrix, which separates the librational and rotational motion. However, looking at the corresponding Lyapunov diagram, we notice that this remains of the separatrix is the source of chaos since $\lambda_1 > 0$, precluding the system's integrability.

After completing the numerical analysis, it is worth revisiting the Lyapunov exponents diagram shown in Fig. 5(d). For the parameters (3.1) and $\omega = 100$, the original system (2.6) has zero Lyapunov exponents for any initial condition. In Fig. 19, we show the Poincaré cross-section of six-dimensional system (2.6) restricted to $(\varphi_2, \omega_2, \varphi_1)$ -space and its projection to (φ_2, ω_2) -plane. As we can notice, for the sufficiently high value of ω , which implies that the gravitational potential is much stronger than Hooke's potential, the double spring pen-

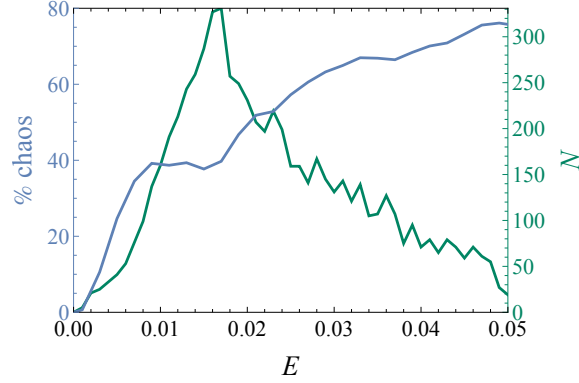


Figure 16: (Color online) The percentage of chaos against the number of stable periodic orbits in the Poincaré section planes a function of energy

dulum possesses integrable dynamics. In contrast to previously examined Poincaré sections, all six Lyapunov exponents are zero up to a value of λ_1 less than 0.002. Additionally, due to the small amplitude of oscillations of the first pendulum, i.e., $\varphi_1 \in [-0.06\pi, 0.06\pi]$, the projection of 3D Poincaré section to (φ_2, ω_2) -plane appears to be that of a like standard Poincaré section for a Hamiltonian system with two degrees of freedom.

4. Integrability analysis

The numerical analysis exemplified by the bifurcation diagrams, the Poincaré sections as well as by the Lyapunov exponent diagrams show complex and, in fact, chaotic dynamics of the considered model. However, it is important to note that the numerical analysis was conducted only for fixed parameter values. For different parameters, the results can be significantly different, and in some cases, the system may have a first integral and be integrable. To fully analyze the integrability of the system (2.6), we employ the Morales-Ramis theory [51]. This theory examines the differential Galois group of variational equations derived from the linearization of equations of motion along a particular solution. The main theorem of this theory states that if the Hamiltonian system is integrable in the Liouville sense, then the identity component of the differential Galois group of variational equations must be Abelian. For this article, we mention only the basic facts of this theory concerning the connection between the integrability of Hamiltonian systems with the differential Galois theory. For a detailed description of the Morales-Ramis theory and the Kovacic algorithm, see the papers [12, 51, 52, 67]. We also refer to the recent results obtained by Combot and Sanabria in the paper [70], where the extension of the Kovacic algorithm to the fourth-order linear differential equations is given.

Below we formulate the main theorem of this paper.

Theorem 4.1. *Let μ, δ and ω are positive parameters. Then, the double spring pendulum system governed by Lagrange function (2.5) is not integrable in the class of functions meromorphic in coordinates and velocities.*

4.1. Outline of the proof

System (2.6) possesses the following invariant manifold

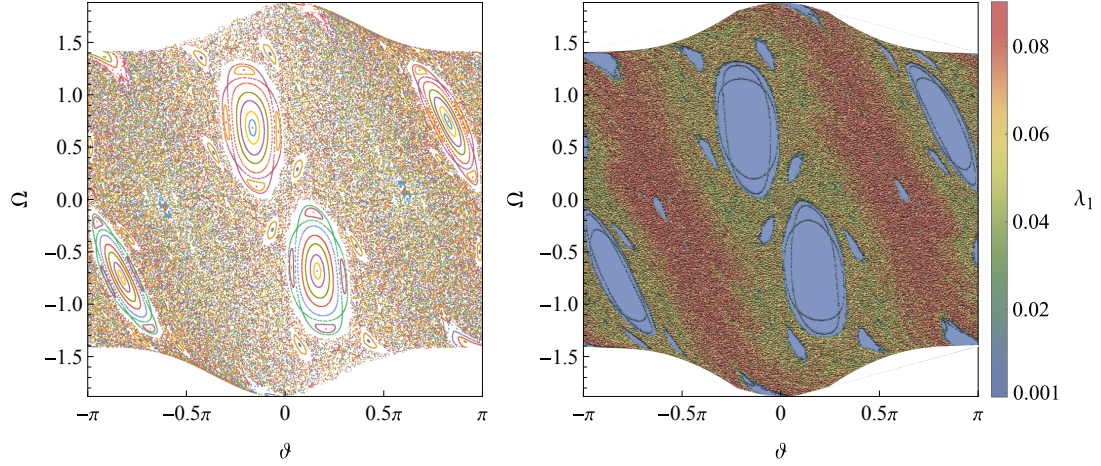
$$\mathcal{N} = \{(\ell, v, \varphi_1, \omega_1, \varphi_2, \omega_2) \in \mathbb{R}^6 \mid \varphi_1 = \omega_1 = 0 = \varphi_2 = \omega_2\}. \quad (4.1)$$

Restricting the right-hand sides of (2.6) to \mathcal{N} , we get equations for the harmonic oscillator

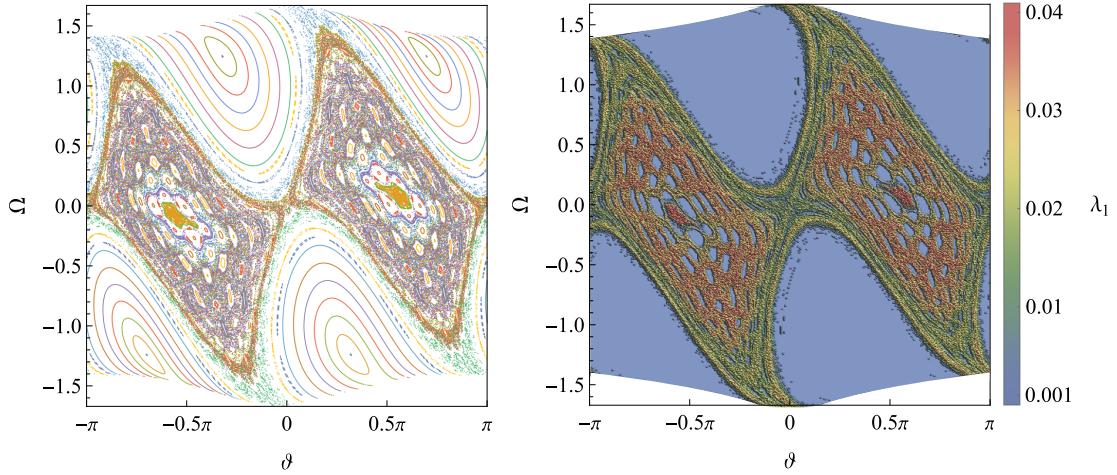
$$\dot{\ell} = v, \quad \dot{v} = \delta + \omega - \ell, \quad \dot{\varphi}_1 = \dot{\omega}_1 = \dot{\varphi}_2 = \dot{\omega}_2 = 0, \quad (4.2)$$

with the energy first integral

$$E = \frac{v^2}{2} + \frac{\ell^2}{2} - \delta\ell - \omega\ell. \quad (4.3)$$

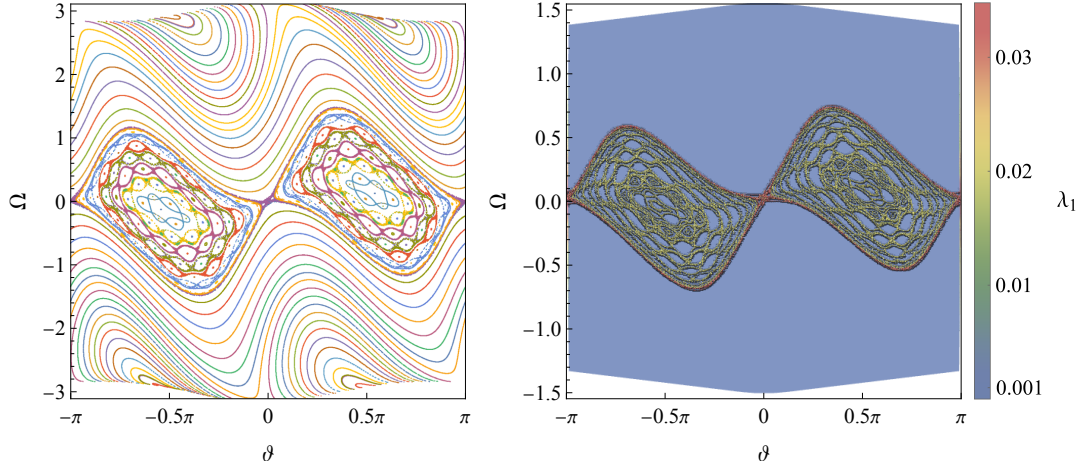


(a) Mass ratio $\mu = 5$, highly chaotic dynamics

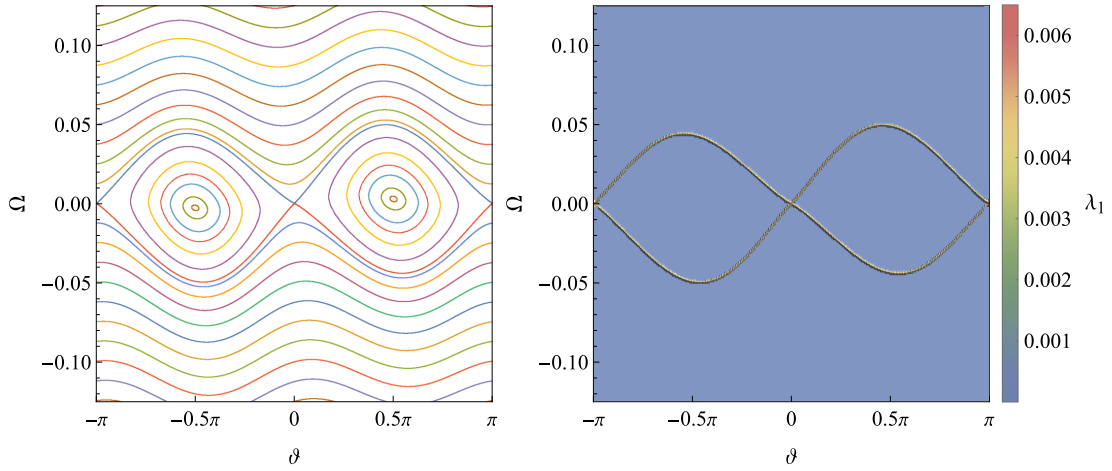


(b) Mass ratio $\mu = 10$, the rise of regular islands between chaotic layers

Figure 17: (Color online) The Poincaré sections of the system (3.7) and their corresponding Lyapunov diagrams, constructed for constant values of the parameters $\delta = 1$, $c = 0$, at the energy level $E = E_0 + 0.5$ where $E_0 = 0$ is the energy minimum, with gradually increasing values of the mass ratio μ . The cross-section plane was defined as $\ell = 1$ with the direction $v > 0$. In the Poincaré sections, the colors are associated with different classical trajectories. For the Lyapunov exponents, the color code is given on the bar. Blue regions indicate regular dynamics, while regions with $\lambda_1 > 0$ correspond to the system's chaotic behavior



(a) Mass ratio $\mu = 15$, decreasing of chaotic area



(b) Mass ratio $\mu = 50$, the almost integrable dynamics

Figure 18: (Color online) The Poincaré sections of the system (3.7) and their corresponding Lyapunov diagrams, constructed for constant values of the parameters $\delta = 1$, $c = 0$, at the energy level $E = E_0 + 0.5$ where $E_0 = 0$ is the energy minimum, with gradually increasing values of the mass ratio μ . The cross-section plane was defined as $\ell = 1$ with the direction $v > 0$. In the Poincaré sections, the colors are associated with different classical trajectories. For the Lyapunov exponents, the color code is given on the bar. Blue regions indicate regular dynamics, while regions with $\lambda_1 > 0$ correspond to the system's chaotic behavior

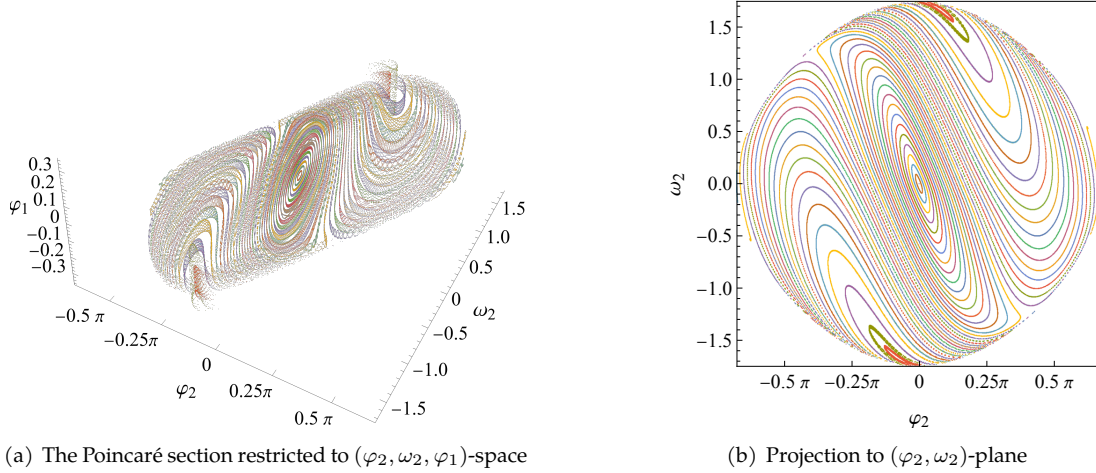


Figure 19: The Poincaré cross-section of the original system (2.6) made for constant values of the parameters $\mu = 3$, $\delta = 1$, $\omega = 100$. The cross-section plane was defined as $\ell = 1$ with the direction $v > 0$. The plot indicates regular, almost integrable dynamics. Each color at the Poincaré plane corresponds to distinct initial conditions

Hence, solving equations (4.2) and taking into account (4.3), we obtain a family of particular solutions $\varphi(t) = (\ell(t, E), v(t, E), 0, 0, 0, 0)$.

Let $\mathbf{X} = [L, V, \Phi_1, \Omega_1, \Phi_2, \Omega_2]^T$ denote the variations of $\mathbf{x} = [\ell, v, \varphi_1, \omega_1, \varphi_2, \omega_2]^T$. Then, the variational equations of system (2.6) along $\varphi(t)$, are as follows

$$\dot{\mathbf{X}} = \mathbf{J}(t) \cdot \mathbf{X}, \quad \text{where} \quad \mathbf{J}(t) = \frac{\partial \mathbf{v}}{\partial \mathbf{x}}(\varphi(t)). \quad (4.4)$$

Here v denotes the right-hand side of system (2.6). The explicit form of the non-constant matrix \mathbf{J} is given by

$$\mathbf{J}(t) = \begin{pmatrix} 0 & 1 & 0 & 0 & 0 & 0 \\ -1 & 0 & 0 & 0 & 0 & 0 \\ 0 & 0 & 0 & 1 & 0 & 0 \\ 0 & 0 & \frac{\delta - \mu\omega - \ell(t)}{\mu} & 0 & \frac{-\delta + \ell(t)}{\mu} & 0 \\ 0 & 0 & 0 & 0 & 0 & 1 \\ 0 & 0 & \frac{-\delta + \mu\omega + \ell(t)}{\mu\ell(t)} & 0 & \frac{\delta - \mu\omega - \ell(t)}{\mu\ell(t)} & -\frac{2v(t)}{\ell(t)} \end{pmatrix}. \quad (4.5)$$

We notice that variational equations separate into blocks: normal variational equations for variables $[\Theta_1, \Omega_1, \Theta_2, \Omega_2]^T$ and tangential equations for variables $[L, V]^T$. Because the tangential system is trivially solvable, for further integrability analysis we take the normal part, which has the form

$$\begin{pmatrix} \dot{\Phi}_1 \\ \dot{\Omega}_1 \\ \dot{\Phi}_2 \\ \dot{\Omega}_2 \end{pmatrix} = \begin{pmatrix} 0 & 1 & 0 & 0 \\ \frac{\delta - \mu\omega - \ell(t)}{\mu} & 0 & \frac{-\delta + \ell(t)}{\mu} & 0 \\ 0 & 0 & 0 & 1 \\ \frac{-\delta + \mu\omega + \ell(t)}{\mu\ell(t)} & 0 & \frac{\delta - \mu\omega - \ell(t)}{\mu\ell(t)} & -\frac{2v(t)}{\ell(t)} \end{pmatrix} \begin{pmatrix} \Phi_1 \\ \Omega_1 \\ \Phi_2 \\ \Omega_2 \end{pmatrix}. \quad (4.6)$$

This system can be written as a one fourth-order differential equation

$$\ddot{\ddot{\Phi}}_1 + a_3(t)\ddot{\Phi}_1 + a_2(t)\dot{\Phi}_1 + a_1(t)\dot{\Phi}_1 + a_0(t)\Phi_1 = 0, \quad (4.7)$$

with time-dependent coefficients

$$\begin{aligned}
a_3(t) &= \left(\frac{2\delta v}{(\delta - \ell)\ell} \right), \\
a_2(t) &= \left(1 + \frac{1 - \delta}{\mu} + \omega - \frac{\delta + 2\delta\mu + 3\mu\omega}{\mu\ell} + \frac{3\omega}{\ell - \delta} + \frac{\ell}{\mu} \right), \\
a_1(t) &= 2 \left(\frac{1}{\mu} + \frac{\omega}{\delta - \ell} + \frac{\mu\omega - \delta}{\mu\ell} \right), \\
a_0(t) &= \omega \left(1 + \frac{1}{\mu} + \frac{3\omega}{\ell - \delta} - \frac{\delta + 2\delta\mu + 3\mu\omega}{\mu\ell} \right).
\end{aligned} \tag{4.8}$$

Lemma 1. *Let us assume $\omega = 0$, then the fourth-order differential equation (4.7) factorizes, i.e., coincides with the action $L_1[L_2[L_3\Phi_1(t)]] = 0$, where L_i are differential operators defined as*

$$\begin{aligned}
L_1 &= \frac{d}{dt} + \left(\frac{v}{\ell} + \frac{v}{1 + \ell} + \frac{v}{\delta - \ell} \right), \\
L_2 &= \frac{d^2}{dt^2} + \left(\frac{v}{\ell} - \frac{v}{1 + \ell} + \frac{v}{\delta - \ell} \right) \frac{d}{dt} - \frac{(1 + \mu + \ell(2 + \ell))(\delta - \ell)}{\mu(1 + \ell)\ell}, \\
L_3 &= \frac{d}{dt}.
\end{aligned} \tag{4.9}$$

Proof. Explicit computations are straightforward but lengthy, so we leave this to the interested reader. \square

We split our further integrability analysis into two independent cases, i.e., when $\omega \neq 0$ and $\omega = 0$.

Case with $\omega \neq 0$

To begin with, we change the independent variable in the variational equation (4.7) by substituting

$$t \rightarrow z = \frac{1}{\ell(t) - \delta}, \quad \text{with} \quad E = -\frac{1}{2}\delta(\delta + 2\omega). \tag{4.10}$$

Taking into account the transformation rules for derivatives, we obtain an equation of the following form

$$y^{(4)} + a_3(z)y''' + a_2(z)y'' + a_1(z)y' + a_0(z)y = 0, \tag{4.11}$$

where $y = \Phi_1(t(z))$ and a_i are rational coefficients defined as

$$\begin{aligned}
a_3(z) &= \frac{6}{z} + \frac{3}{z - z_1} + \frac{2}{z - z_2}, \\
a_2(z) &= \frac{3}{16\omega^2 z^2 (z - z_1)^2} + \frac{117\delta z^2 + 2\delta z + 75z + 2}{4\delta z^3 (z - z_2)} + \frac{\mu + \mu(\delta + 32\delta z + 27)z + 2(\delta + 1)z + 2}{4\delta\mu\omega z^3 (z - z_1)(z - z_2)}, \\
a_1(z) &= \frac{63\delta z^2 + 7\delta z + 30z + 3}{4\delta z^4 (z - z_2)} + \frac{\mu + \mu(\delta + 5\delta z + 6)z + 2(\delta + 1)z + 2}{16\delta\mu\omega^2 z^4 (z - z_1)^2 (z - z_2)} \\
&\quad + \frac{2\mu + [18\mu + ((4 + 26z)\mu + 3)\delta + 3]z - 1}{4\delta\mu\omega z^4 (z - z_1)(z - z_2)}, \\
a_0(z) &= \frac{3}{4z^4 (z - z_2)} + \frac{2\mu + \delta\mu z + 2}{16\delta\mu\omega^2 z^5 (z - z_2)(z - z_1)^2} + \frac{\mu + 2\delta\mu z + 1}{4\delta\mu\omega z^5 (z - z_1)(z - z_2)}.
\end{aligned} \tag{4.12}$$

The non-integrability proof of the system is based on the necessary conditions formulated in Lemma 7 contained in the appendix. Therefore, we need to first check whether equation (4.11) has a hyperexponential solution. A function $f(z)$ is called hyperexponential if its logarithmic derivative $f'(z)/f(z)$ is a rational function. We will now proceed to prove the following.

Lemma 2. *Equation (4.11) does not admit any hyperexponential solution.*

Proof. If $\omega\delta \neq 0$, then equation has four distinct singular points

$$z_0 = 0, \quad z_1 = \frac{1}{2\omega}, \quad z_2 = -\frac{1}{\delta}, \quad z_\infty = \infty. \quad (4.13)$$

Singularities z_1, z_2 and z_∞ are regular singular points, while point z_0 is irregular. The exponents at these points are as follows

$$E_1 = \{0, 1/2, 1, 3/2\}, \quad E_2 = \{0, 1, 2\}, \quad E_\infty = \{0, 1/2, 2, 5/2\}.$$

Using Maple, we found that the exponential parts of formal solutions are following

$$\mathcal{E}(z) \in \{1, z^2, z^{1/4} \exp[\pm 2/\sqrt{\mu z}]\}. \quad (4.14)$$

Looking for a hyperexponential solution only first has to be considered. The first one also has to be rejected because in this case the formal solution is logarithmic, that is

$$\hat{y}(z) = c_0(z) + c_1(z) \ln(z), \quad (4.15)$$

and $c_1(z)$ vanishes identically only if $\omega(\delta + \mu + 1) = 0$. Hence, if it exists, it has the form

$$y(z) = P(z) \prod_{i=0}^2 (z - z_i)^{e_i}, \quad e_i \in E_i, \quad (4.16)$$

where $E_0 = \{0, 2\}$. Now, the degree d of the polynomial $P(z)$ must be $d = -e_0 - e_1 - e_2 - e_\infty$, where $e_0 = 2$. Thus, $d \leq -2$ for an arbitrary $e_i \in E_i$ with $i = 1, 2, \infty$. This ends the proof. \square

To check the second assumption of Lemma 7, we have to analyze the second exterior power of equation (4.11), that is, the corresponding system (A.5). Rewritten as a scalar equation, it has order six, and it reads

$$\sum_{i=0}^6 b_i(z) w^{(i)} = 0, \quad (4.17)$$

where coefficients $b_i(z)$ are rational functions, but they are rather long, so we do not write them here explicitly. This equation has five regular singular points

$$z_1 = \frac{\omega}{2}, \quad z_2 = -\frac{1}{\delta}, \quad z_{3,4} = \pm \frac{1}{\sqrt{\mu\omega\delta}}, \quad z_\infty = \infty. \quad (4.18)$$

The exponents at these points belong to the respective sets

$$\begin{aligned} E_1 &= \{-1/2, 0, 1/2, 1, 3/2, 5/2\}, & E_2 &= \{0, 1, 2, 3\} \\ E_{3,4} &= \{0, 1, 2, 3, 4, 6\}, & E_\infty &= \{3/2, 3, 7/2, 4, 9/2, 11/2\}. \end{aligned} \quad (4.19)$$

The point $z = 0$ is irregular. Of the six formal solutions, only two can be taken into account when looking for hyperexponential solutions. Their exponential parts are $\mathcal{E}(z) \in \{z^{-1}, z\}$. In effect, there is only one possibility for the exponential solution of equation (4.17), namely $w(z) = 1/z\sqrt{z - z_1}$, and it is a solution of these equations.

In the above, we assumed that all the singular points are pairwise different. It is possible that for certain choices of parameters, their number is smaller. For example, if $\delta = \mu\omega$ then $z_2 = z_3$. An analysis of all these cases showed that equation (4.17) has always just one hyper-exponential solution of the form given above.

Case with $\omega = 0$

For $\omega = 0$ it is appropriate to make a linear change of the variational variables in (4.6). Namely,

$$\begin{aligned} X_1 &= \Phi_1 + \Phi_2, & Y_1 &= \Omega_1 + \Omega_2, \\ X_2 &= \Phi_1 - \Phi_2, & Y_2 &= \Omega_1 - \Omega_2. \end{aligned} \quad (4.20)$$

The normal variational equations (4.6) in variables (X, U, Y, V) take the form

$$\begin{pmatrix} \dot{X}_1 \\ \dot{Y}_1 \\ \dot{X}_2 \\ \dot{Y}_2 \end{pmatrix} = \begin{pmatrix} 0 & 1 & 0 & 0 \\ 0 & -\frac{v}{\ell} & \frac{(v-\ell)(\ell-1)}{\mu\ell} & \frac{v}{\ell} \\ 0 & 0 & 0 & 1 \\ 0 & \frac{v}{\ell} & \frac{(v-\ell)(\ell+1)}{\mu\ell} & -\frac{v}{\ell} \end{pmatrix} \begin{pmatrix} X_1 \\ Y_1 \\ X_2 \\ Y_2 \end{pmatrix}. \quad (4.21)$$

We can notice that the equations for (Y_1, X_2, Y_2) do not depend on the variable X_1 , that is, the variable X_1 decouples from the remaining variables. Thus, it is sufficient to investigate the subsystem of variables (Y_1, X_2, Y_2) . Moreover, this subsystem has the first integral

$$F = \frac{1}{2} (1 + \mu + 2\ell + \ell^2) Y_1 + \frac{1}{2} (1 + \mu - \ell^2) Y_2 - v X_2. \quad (4.22)$$

At level $F = 0$, we have

$$Y_1 = \frac{2v X_2 - (1 + \mu - \ell^2) Y_2}{1 + \mu + 2\ell + \ell^2}. \quad (4.23)$$

Therefore, we can eliminate the variable Y_1 , and we end up with the system for the variables (X_2, Y_2) . It can be rewritten as a one-second-order differential equation

$$\ddot{y} + a(t)\dot{y} + b(t)y = 0, \quad y \equiv X_2, \quad (4.24)$$

where

$$a(t) = \frac{2(1 + \mu + \ell)v}{\ell(1 + \mu + 2\ell + \ell^2)}, \quad b(t) = \frac{(1 + \ell)(\ell - \delta)}{\mu\ell} + \frac{2(\delta - \ell)^2}{\ell(1 + \mu + 2\ell + \ell^2)}. \quad (4.25)$$

Then, we make the following change of the independent variable $t \rightarrow z = \ell(t)$. Taking into account the transformation rules for the derivatives, we transform (4.24) into the equation with rational coefficients

$$y'' + p(z)y' + q(z)y = 0, \quad ' \equiv \frac{d}{dz}. \quad (4.26)$$

Explicit forms of coefficients $p(z)$ and $q(z)$ are given by

$$p(z) = \frac{2}{z} + \frac{1}{z - \delta} - \frac{2(z + 1)}{(z + 1)^2 + \mu}, \quad q(z) = -\frac{z + 1}{\mu z(z - \delta)} - \frac{2}{z((z + 1)^2 + \mu)}. \quad (4.27)$$

Now, we make the classical Tschirnhaus change of the dependent variable

$$y(z) = x(z) \exp \left[-\frac{1}{2} \int p(z) \right], \quad (4.28)$$

which converts (4.26) into its reduced form

$$x'' = r(z)x, \quad (4.29)$$

with rational coefficient

$$r(z) = -\frac{1}{4(z - z_1)^2} - \frac{3\mu}{(z - z_2)^2(z - z_3)^2} + \frac{(z + 1)^3 + 2\mu(z + 1) + \mu^2}{\mu z(z - z_1)(z - z_2)(z - z_3)}. \quad (4.30)$$

Equation (4.29) has five singularities

$$z_0 = 0, \quad z_1 = \delta, \quad z_{2,3} = -1 \pm i\sqrt{\mu}, \quad z_\infty = \infty. \quad (4.31)$$

The singularity z_0 is a pole of the first order, while $\{z_1, z_2, z_3\}$ are poles of the second order. The degree of infinity is one. Taking into account the characters of singularities, we deduce that differential Galois group of reduced equation (4.29) cannot be reducible (first case of the Kovacic algorithm) or finite (the third case of the Kovacic algorithm). The differential Galois group can be only dihedral (case 2 of the Kovacic algorithm) or whole $SL(2, \mathbb{C})$. To distinguish between these cases, we apply the Kovacic algorithm.

Lemma 3. *The differential Galois group of Eq. (4.29) is $SL(2, \mathbb{C})$.*

Proof. According to the second case of the Kovacic algorithm, for singularities $\{z_1, z_2, z_3\}$ with order two, we define sets of exponents

$$E_i = \{2, 2 \pm 2\sqrt{1 + 4c_i}\} \cap \mathbb{Z}, \quad i = 1, 2, 3, \quad (4.32)$$

where c_i are coefficients in the dominant terms of the Laurent series expansions of $r(z)$ around z_i . Because z_0 and z_∞ are singularities of order one, we define $E_0 = \{4\}$ and $E_\infty = \{1\}$. Hence, the explicit forms of the auxiliary sets E_i are given by

$$E_0 = \{4\}, \quad E_1 = \{2, 2, 2\}, \quad E_2 = \{-2, 2, 6\}, \quad E_3 = \{-2, 2, 6\}, \quad E_\infty = \{1\}. \quad (4.33)$$

Next, following the algorithm, we calculate the Cartesian product $E = E_0 \times E_1 \times E_2 \times E_3 \times E_\infty$. From the obtained 27-element list, we look for these permutations $e = (e_0, e_1, e_2, e_3, e_\infty)$ for which

$$d(e) = e_\infty - e_0 - e_1 - e_2 - e_3 \in \mathbb{N}_{\text{even}}. \quad (4.34)$$

However, direct computations show that none of e gives a non-negative $d(e)$. Thus, the algorithm has stopped and the second case of the algorithm does not occur. Therefore, the differential Galois group of Eq. (4.29) is $SL(2, \mathbb{C})$ with a non-Abelian identity component. \square

Following Lemma 7, we have shown that for $\omega \neq 0$ variational equation (4.7) does not possess any hyperexponential solution, and its associate external second power has exactly one hyperexponential solution. Therefore, for $\omega \neq 0$ the double spring pendulum is not integrable in a class of functions meromorphic in coordinates and velocities. Moreover, for $\omega = 0$, we have shown that the variational equations are reduced to the one second-order differential equation for which the differential Galois group is $SL(2, \mathbb{C})$ with non-Abelian identity component. Therefore, we conclude that the double spring pendulum system governed by the Lagrange function (2.5) is not integrable in a class of meromorphic functions in coordinates and velocities for all values of the parameters. This ends the proof.

5. Summary and conclusions

The complicated and mostly chaotic dynamics of multiple pendulums is well known but still in a great scientific activity. This is because such systems explain many fundamental phenomena and have found applications in engineering, robotics, and synchronization theory. Currently, we can observe an increase in the work on the study of dynamics and chaos in multiple pendulums of variable length. Compared to classic pendulums, these pendulums have variable arms lengths, making their analysis a quite challenging task since they usually have many degrees of freedom and their corresponding differential equations are highly non-linear. As a result, the study of these systems may lead to the discovery of new phenomena related to chaos theory, which is particularly interesting from a scientific point of view. It is also worth noting that chaotic and chaotic phenomena can appear in variable-length systems even for very small perturbations of the parameters. This poses a challenge for researchers analyzing the stability of dynamical systems.

In this paper, we studied the dynamics and integrability of the variable-length pendulum system, such as the double spring pendulum. It is a Hamiltonian system with three degrees of freedom, so its analysis was quite a challenging task. To gain insight into the dynamics of the system, we joined various numerical methods to get the most reliable results. By joining the Lyapunov exponents with the bifurcation diagrams and Poincaré sections as one powerful tool, we gave a complete picture of the system dynamics by specifying values of parameters or initial conditions for which motion of the studied model can be hyperchaotic, chaotic, quasi-periodic, and finally periodic, which is completely new in the context of Hamiltonian systems. Moreover, in the absence of gravitational potential, the system exhibits S^1 symmetry, and the presence of an additional first integral was identified using Lyapunov exponents diagrams. We demonstrate the effective utilization of Lyapunov exponents as a potential indicator of first integrals and integrable dynamics.

The detailed analysis suggests the non-integrability of the proposed model, accompanied by analytical proof. The presence of particular solutions allowed us to apply Morales-Ramis theory. The novelty of our work lies in the integrability analysis of the Hamiltonian system with three degrees of freedom, where the variational

equation is transformed into a fourth-order differential equation. To effectively analyze the differential Galois group of variational equations, we employed a recently formulated extension of the Kovacic algorithm designed for dimension four.

In summary, our article presents a comprehensive analysis of the dynamics and integrability of the double spring pendulum, offering new insights and methodologies for further research in this field. We employed powerful tools to obtain results that are of significant importance and usefulness in the study of differential equations, vibrations, and synchronization theory. Variable-length pendulums hold importance from theoretical and practical perspectives, rendering them a fascinating research subject in the field of nonlinear dynamics. Although primarily studied in the realm of nonlinear dynamics and classical mechanics, they have potential applications in various fields, including space debris removal. For instance, the idea for capturing and manipulating debris objects in space mentioned in the introduction can be modeled as a version of a double spring pendulum system. The chaotic nature of the double spring pendulum system shown in this paper presents challenges and opportunities for trajectory planning during debris removal operations. Advanced algorithms for dynamic trajectory optimization could be developed to exploit the system's nonlinear dynamics and chaotic behavior for efficient debris capture and manipulation. Thus, the results obtained in this work could provide qualitative and quantitative information about the possible complex dynamics of the tethered satellite system for active debris removal. Moreover, further studies of the double spring pendulum with some additional dissipations could provide important information about the influence of atmospheric disturbance on the dynamics of tethered satellite system. By continuously adapting the system's parameters in response to changing environmental conditions and debris characteristics, optimal trajectories can be calculated to minimize fuel consumption and maximize operational effectiveness.

Declaration of competing interest

The authors declare that they have no known competing financial interests or personal relationships that could have appeared to influence the work reported in this paper.

Acknowledgements

For Open Access, the authors have applied a CC-BY public copyright license to any Author Accepted Manuscript (AAM) version arising from this submission.

Funding

This research was funded by The National Science Center of Poland under Grant No. 2020/39/D/ST1/01632.

Data availability

The data that support the findings of this study are available from the corresponding author, upon reasonable request.

Appendix A. Proof of Theorem

The key point in the application of Morales-Ramis theory is to decide if the differential Galois group of variational equations is virtually Abelian, that is if its identity component is Abelian. In the majority of cases when the theory was implemented, the variational equations split into a set of second-order equations, or had, as a subset, a second-order equation. Furthermore, it was almost always possible to convert these second-order equations into equations with rational coefficients. Therefore, it was possible to use the Kovacic algorithm formulated in [67], which was designed to find the closed form of solutions of the considered second-order equation. More precisely, it decides if the system admits solutions in a field of Liouvillian functions. The algorithm is based on the complete classification of the algebraic subgroups of the group $SL(2, \mathbb{C})$. As a by-product, it determines the differential Galois group of the equation.

Equations of motion of a Hamiltonian system with n degrees of freedom can be written as

$$\dot{z} = \mathbb{J}H'(z), \quad \mathbb{J} = \begin{bmatrix} 0 & \mathbb{I}_n \\ -\mathbb{I}_n & 0 \end{bmatrix}, \quad z = [\mathbf{q}, \mathbf{p}]^T, \quad (\text{A.1})$$

and the corresponding variational equations along a particular solution $\varphi(t)$ are also Hamiltonian

$$\dot{Y} = \mathbb{J}H''(\varphi(t))Y. \quad (\text{A.2})$$

It is easy to show that the differential Galois group of this system is a subgroup of the symplectic group, $\text{Sp}(2n, \mathbb{C})$. For $n = 1$ the group $\text{Sp}(2, \mathbb{C})$ is isomorphic to $\text{SL}(2, \mathbb{C})$. However, for larger dimensions $\text{Sp}(2m, \mathbb{C}) \subset \text{SL}(2m, \mathbb{C})$, it is much smaller than $\text{SL}(2m, \mathbb{C})$. The classification of the subgroups of $\text{Sp}(4, \mathbb{C})$ is known. Among other things, this fact was used in [57] where the equivalent of the Kovacic algorithm for symplectic differential operators of degree four was formulated.

For a brief description of this algorithm, we introduce the appropriate terminology. Let L be a differential operator with coefficients in $\mathbb{C}(z)$

$$L(y) = y^{(n)} + a_{n-1}y^{(n-1)} + \dots + a_1y' + a_0y = 0, \quad a_i \in \mathbb{C}(z), \quad (\text{A.3})$$

and A is its corresponding companion matrix, that is

$$A = \begin{bmatrix} 0 & 1 & 0 & \dots & 0 \\ 0 & 0 & 1 & \dots & 0 \\ \vdots & \vdots & \vdots & \ddots & \vdots \\ 0 & 0 & 0 & \dots & 1 \\ -a_0 & -a_1 & -a_2 & \dots & -a_{n-1} \end{bmatrix}. \quad (\text{A.4})$$

An operator of even order $n = 2n$ is

- symplectic if there exists an invertible skew-symmetric matrix W with elements in $\mathbb{C}(z)$ which is a solution of the following equation

$$A^T W + W A + W' = 0, \quad (\text{A.5})$$

- projectively symplectic, if there exists an invertible skew-symmetric matrix W with elements in $\mathbb{C}(z)$ which is a solution of equation

$$A^T W + W A + W' + \lambda W = 0, \quad (\text{A.6})$$

for a certain $\lambda \in \mathbb{C}(z)$.

An operator L of order $n = 2m$ is symplectic (respectively projectively symplectic) when its Galois group is isomorphic to a subgroup of symplectic matrices $\text{Sp}(2m, \mathbb{C})$ (respectively projectively symplectic matrices $\text{PSP}(2m, \mathbb{C})$)

$$\begin{aligned} \text{Sp}(2m, \mathbb{C}) &= \{M \in \mathbb{M}_{2m}(\mathbb{C}) \mid M^T \mathbb{J} M = \mathbb{J}\}, \\ \text{PSP}(2m, \mathbb{C}) &= \{M \in \mathbb{M}_{2m}(\mathbb{C}) \mid M^T \mathbb{J} M = \lambda \mathbb{J}, \lambda \in \mathbb{C}^*\}. \end{aligned}$$

If L is projectively symplectic, then up to a multiplication of a hyper exponential function, the operator can be symplectic. The function $f(z)$ is called hyper-exponential if its logarithmic derivative $f'(z)/f(z)$ is a rational function.

Lemma 4. *Assume that the system $\dot{x} = Ax$ is symplectic, that is, there exists an invertible skew-symmetric matrix W with coefficients in $\mathbb{C}(z)$ which is a solution of equation (A.5). Then $x(t)$ is a solution of $\dot{x}(t) = Ax(t)$ if and only if $x_*(t) = Wx(t)$ is a solution of the adjoining equation $\dot{x}_*(t) = -A^T x_*(t)$.*

This lemma can be proved by direct check. It follows that if the symplectic operator L has the right factor L_1 , then its adjoining L^* has a right factor \tilde{L}_1 of the same order. Thus, L has the right factor L_1 , then it also has a left factor of the same degree.

With a system $\dot{x} = Ax$, we can associate its external second power. It is a system of the form

$$\dot{W} = AW - W^T A^T \quad (\text{A.7})$$

where W is an antisymmetric matrix. Thus, equation (A.5) is an equation for the external square of a dual system to system $x' = Ax$.

The classification theorem formulated in [57] is the following.

Lemma 5. *A Lie subgroup of $\text{Sp}(4, \mathbb{C})$ is up to conjugacy generated by elements of the form:*

1. upper block triangular matrices with diagonal blocks of size at most 2×2 ,
2. 2×2 diagonal matrices and anti-diagonal matrices

$$\begin{bmatrix} * & * & 0 & 0 \\ * & * & 0 & 0 \\ 0 & 0 & * & * \\ 0 & 0 & * & * \end{bmatrix}, \quad \begin{bmatrix} 0 & 0 & * & * \\ 0 & 0 & * & * \\ * & * & 0 & 0 \\ * & * & 0 & 0 \end{bmatrix},$$

3. full group $\text{Sp}_4(\mathbb{C})$.

This classification is constructed based on the known classification of Lie subgroups of the larger unimodular group $\text{SL}(4, \mathbb{C}) \supset \text{Sp}(4, \mathbb{C})$. Subgroups of the projective symplectic group are central extensions of these, and so contain multiples of the identity matrix with non-unit determinant. However, since these commute with all matrices, the possible structures of subgroups in the items 1, 2 are unchanged.

The next two lemmas characterize the reducible case.

Lemma 6. *Let us consider the following block diagonal system*

$$\dot{x} = Ax \quad A = \begin{bmatrix} B & C \\ 0 & D \end{bmatrix}, \quad (\text{A.8})$$

where B , C and D are matrices 2×2 with rational coefficients. Then the equation (A.5) has the following particular solution

$$W = e^{\int r} \begin{bmatrix} 0 & 0 \\ 0 & J \end{bmatrix}, \quad J = \begin{bmatrix} 0 & 1 \\ -1 & 0 \end{bmatrix}, \quad (\text{A.9})$$

where r is a rational function.

In our proof of non-integrability, we will use the following criterion.

Lemma 7. *Assume that the equation*

$$L(y) = y^{(4)} + a_3(z)y''' + a_2(z)y'' + a_1(z)y' + a_0(z)y = 0, \quad ' = \frac{d}{dz} \quad (\text{A.10})$$

is projectively symplectic and A is its corresponding companion matrix. If (A.10) does not admit a hyper exponential solution and equation (A.5) has exactly one hyper exponential solution, then the differential Galois group of (A.10) contains $\text{Sp}(4, \mathbb{C})$.

Hence, we must know how to check if a given equation has a hyperexponential solution.

If $L(y) = 0$ is of Fuchsian type, then any hyper exponential solution must be of the form $P(z) \prod_i (z - z_i)^{e_i}$, where $P(z) \in \mathbb{C}[z]$, $z_i \in \mathbb{C}$ is a singular point, e_i are exponents at z_i . Then, the necessary conditions for such a solution is given in Lemma 3.1 in [68]. As a corollary, we have the following.

Proposition Appendix A.1. *If a Fuchsian equation of order four has a factor of order one, then either $L(y) = 0$ or $L^*(y) = 0$ has a solution of the form $P(z) \prod_i (z - z_i)^{e_i}$, where $P(z) \in \mathbb{C}[z]$, $z_i \in \mathbb{C}$ are singularities, e_i are exponents at z_i , and there exists an exponent at infinity e_∞ such that the sum $\sum_i e_i + e_\infty$ is a non-positive integer.*

For an equation $L(y) = 0$ which is not Fuchsian, the conditions for the existence of a hyperexponential solution is more complicated. We consider only a particular case, assuming that equation $L(y) = 0$ has only one irregular singular point at $z = 0$. Then its hyperexponential solution must be of the form

$$y(z) = \mathcal{E}(z)R(z) \prod_{i=1}^m (z - z_i)^{e_i}, \quad (\text{A.11})$$

where $R(z)$ is a rational function, $z_i \in \mathbb{C}$ is a singular point, e_i are exponents at z_i for $i = 1, \dots, m$. The function $\mathcal{E}(z)$ is an exponential part of a formal solution at the irregular point $z = 0$

$$\widehat{y}(z) = \mathcal{E}(z) \left[c_0(z^{1/k}) + c_1(z^{1/k}) \ln(z) + \dots + c_m(z^{1/k}) \ln(z)^m \right] \quad (\text{A.12})$$

where

$$\mathcal{E}(z) = \exp[W(z^{-1/k})]z^a, \quad (\text{A.13})$$

W is a polynomial, $k > 0$ and $m \geq 0$, $a \in \mathbb{C}$ and c_i are formal power series. In practice, formal solutions can be found with the help of a computer algebra system, for example, MAPLE.

For the equation of order n , there are n linearly independent solutions of this form. For formula (A.11) we take only those for which $k = 1$ and $m = 0$. If the exponential part is $\mathcal{E}(z) = z^a$, then a is an exponent at a singular point $z = 0$. In this case, if a hyperexponential exists it has the same form as for Fuchsian equation.

References

- [1] W. Szumiński, A. J. Maciejewski, Dynamics and non-integrability of the double spring pendulum. *J. Sound Vib.*, 589:118550, 2024.
- [2] P. A Broucke, R. nad Baxa. Periodic solutions of a spring-pendulum system. *Celestial Mech. Dyn. Astron.*, 8:261–267, 1973.
- [3] W. K. Lee and H. D. Park. Chaotic dynamics of a harmonically excited spring-pendulum system with internal resonance. *Nonlinear Dyn.*, 14(3):211–229, 1997.
- [4] A. J. Maciejewski, M. Przybylska, and J.-A. Weil. Non-integrability of the generalized spring-pendulum problem. *J. Phys. A*, 37(7):2579–2597, 2004.
- [5] J. Awrejcewicz and A. G. Petrov. Nonlinear oscillations of an elastic two-degrees-of-freedom pendulum. *Nonlinear Dyn.*, 53(1-2):19–30, 2008.
- [6] A. Amer, T. S. Amer, and H. F. El-Kafly. Dynamical analysis for the motion of a 2DOF spring pendulum on a lissajous curve. *Sci Rep*, 13:21430, 2023.
- [7] M. Wojna, A. Wijata, G. Wasilewski, and J. Awrejcewicz. Numerical and experimental study of a double physical pendulum with magnetic interaction. *J. Sound Vib.*, 430:214–230, 2018.
- [8] A. Zhang, V. Sorokin, and H. Li. Dynamic analysis of a new autoparametric pendulum absorber under the effects of magnetic forces. *J. Sound Vib.*, 485:115549, 2020.
- [9] S. Skurativskiy, K. Polczyński, M. Wojna, and J. Awrejcewicz. Quantifying periodic, multi-periodic, hidden and unstable regimes of a magnetic pendulum via semi-analytical, numerical and experimental methods. *J. Sound Vib.*, 524:116710, 2022.
- [10] T. Shinbrot, C. Grebogi, J. Wisdom, and J. A. Yorke. Chaos in a double pendulum. *Am. J. Phys.*, 60(6):491–499, 06 1992.
- [11] T. Stachowiak and T. Okada. A numerical analysis of chaos in the double pendulum. *Chaos, Solitons Fractals*, 29(2):417–422, 2006.

- [12] M. Przybylska and W. Szumiński. Non-integrability of flail triple pendulum. *Chaos Soliton. Fract.*, 53:60–74, 2013.
- [13] T. Stachowiak and W. Szumiński. Non-integrability of restricted double pendula. *Phys. Lett. A*, 379(47-48):3017–3024, 2015.
- [14] V. Puzyrov, J. Awrejcewicz, N. Losyeva, and N. Savchenko. On the stability of the equilibrium of the double pendulum with follower force: Some new results. *J. Sound Vib.*, 523:116699, 2022.
- [15] S.I. Nigmatullin, R.R. Osokin and J. et al Awrejcewicz. Application of the generalized prony spectrum for extraction of information hidden in chaotic trajectories of triple pendulum. *Centr.eur.j.phys*, 12:565–577, 2014.
- [16] L. Jahn, B. Watermann and J. Reger. On the design of stable periodic orbits of a triple pendulum on a cart with experimental validation. *Automatica J. IFAC*, 125:Paper No. 109403, 7, 2021.
- [17] T. S. Amer, A. A. Galal, and A. F. Abolila. On the motion of a triple pendulum system under the influence of excitation force and torque. *Kuwait J. Sci.*, 48(4):17, 2021.
- [18] V. Puzyrov, J. Awrejcewicz, N. Losyeva, and N. Savchenko. On the stability of the equilibrium of the double pendulum with follower force: Some new results. *J. Sound Vib.*, 523:116699, 2022.
- [19] S. Dyk, J. Rendl, L. Smolik, and R. Bulin. Energy-based analysis of quadratically coupled double pendulum with internal resonances. *J. Sound Vib.*, 577:118343, 2024.
- [20] H. N. Huynh and L. Y. Chew. Two-coupled pendulum system: Bifurcation, chaos and the potential landscape approach. *Int. J. Bifurcation Chaos*, 20(8):2427–2442, 2010.
- [21] H. N. Huynh, T. P. T. Nguyen, and L. Y. Chew. Numerical simulation and geometrical analysis on the onset of chaos in a system of two coupled pendulums. *Commun. Nonlinear Sci. Numer. Simul.*, 18(2):291–307, 2013.
- [22] A. A. Elmandouh. On the integrability of the motion of 3d-swinging atwood machine and related problems. *Phys. Lett. A*, 380(9):989–991, 2016.
- [23] W. Szumiński and Dariusz Woźniak. Dynamics and integrability analysis of two pendulums coupled by a spring. *Commun. Nonlinear Sci. Numer. Simul.*, 83:105099, 2020.
- [24] W. Szumiński. A new model of variable-length coupled pendulums: from hyperchaos to superintegrability. *Nonlinear Dyn.*, 112:4117–4145, 2024.
- [25] N. Tufillaro, T. A. Abbott, and D. J. Griffiths. Swinging Atwood’s Machine. *Amer. J. Phys.*, 52(52):895–903, 1984.
- [26] N. Tufillaro. Motions of a swinging Atwood’s machine. *J. Physique*, 46(9):1495–1500, 1985.
- [27] J. Casasayas, A. Nunes, and N. Tufillaro. Swinging Atwood’s machine: integrability and dynamics. *J. Physique*, 51(16):1693–1702, 1990.
- [28] W. Szumiński and A.J. Maciejewski. Dynamics and integrability of the swinging Atwood machine generalisations. *Nonlinear Dyn.*, 110:2101–2128, 2022.
- [29] P. Olejnik, G. Yakubu, and K. et al. Pepa. A double variable-length pendulum with counterweight mass, kinematic excitation and electromagnetic forcing. *Nonlinear Dyn*, 111:19723–19747, 2023.
- [30] R. B. Levien and S. M. Tan. Double pendulum: An experiment in chaos. *Am. J. Phys.*, 61(11):1038–1044, 11 1993.
- [31] O. Pujol, J. P. Pérez, J. P. Ramis, C. Simó, S. Simon, and J. A. Weil. Swinging Atwood machine: experimental and numerical results, and a theoretical study. *Phys. D*, 239(12):1067–1081, 2010.

- [32] E. R. Gomez, I. Lopez Arteaga, and L. Kari. Normal-force dependant friction in centrifugal pendulum vibration absorbers: Simulation and experimental investigations. *J. Sound Vib.*, 492:115815, 2021.
- [33] M. Ciezkowski. Dynamic stabilization and feedback control of the pendulum in any desired position. *J. Sound Vib.*, 491:115761, 2021.
- [34] V. N. Pilipchuk, K. Polczyński, M. Bednarek, and J. Awrejcewicz. Guidance of the resonance energy flow in the mechanism of coupled magnetic pendulums. *Mech. Mach. Theory*, 176:105019, 2022.
- [35] W. Chu, C. Li, and G. Zhang. An active continuous control method and its experiment on the rapid suppression of inverted pendulum structure oscillation. *J. Sound Vib.*, 521:116691, 2022.
- [36] M. Wojna, A. Wijata, G. Wasilewski, and J. Awrejcewicz. Numerical and experimental study of a double physical pendulum with magnetic interaction. *J. Sound Vib.*, 430:214–230, 2018.
- [37] F. Liu, B. Yue, Y. Tang, and M. Deng. 3dof-rigid-pendulum analogy for nonlinear liquid slosh in spherical propellant tanks. *J. Sound Vib.*, 460:114907, 2019.
- [38] H. Sharghi and O. Bilgen. Energy harvesting from human walking motion using pendulum-based electromagnetic generators. *J. Sound Vib.*, 534:117036, 2022.
- [39] H. Yang, B. Wu, J. Li, Yu Bao, and G. Xu. A spring-loaded inverted pendulum model for analysis of human-structure interaction on vibrating surfaces. *J. Sound Vib.*, 522:116727, 2022.
- [40] R. Dilão. Antiphase and in-phase synchronization of nonlinear oscillators: The Huygens’s clocks system. *Chaos*, 19(2), 05 2009. 023118.
- [41] P. Koluda, P. Perlikowski, K. Czołczyński, and T. Kapitaniak. Synchronization configurations of two coupled double pendula. *Commun. Nonlinear Sci. Numer. Simul.*, 19(4):977–990, 2014.
- [42] D. Dudkowski, K. Czołczyński, and T. Kapitaniak. Synchronization of two self-excited pendula: Influence of coupling structure’s parameters. *Mech. Syst. Signal Process.*, 112:1–9, 2018.
- [43] Rajarshi R. and K. Scott T. Experimental synchronization of chaotic lasers. *Phys. Rev. Lett.*, 72:2009–2012, Mar 1994.
- [44] M. Shibuya, T. Suzuki, and K. Ohnishi. Trajectory planning of biped robot using linear pendulum mode for double support phase. In *IECON 2006 - 32nd Annual Conference on IEEE Industrial Electronics*, pages 4094–4099, 2006.
- [45] Sahi n Y. Bipedal-double-pendulum walking robot control using recurrent hybrid neural network. *The Inverted Pendulum in Control Theory and Robotics: From theory to new innovations*, Chap. 11, pp. 263-282, 2017.
- [46] A. Vitt and G. Gorelik. Oscillations of an elastic pendulum as an example of the oscillations of two parametrically coupled linear systems. *Zh. Tekh. Fiz.*, 33:294–307, 1933.
- [47] E. A. Lacombe and J. Llibre, editors. *New trends for Hamiltonian systems and Celestial Mech. Dyn. Astron*, volume 8 of *Advanced Series in Nonlinear Dynamics*. World Scientific Publishing Co., Inc., River Edge, NJ, 1996. Papers from the 2nd International Symposium on Hamiltonian Systems and Celestial Mech. Dyn. Astron held in Cocoyoc, September 13–17, 1994.
- [48] P. Lynch. The swinging spring: a simple model of atmospheric balance. In *Large-scale atmosphere-ocean dynamics, Vol. II*, pages 64–108. Cambridge Univ. Press, Cambridge, 2002.
- [49] Peter Lynch and Conor Houghton. Pulsation and precession of the resonant swinging spring. *Phys. D*, 190(1-2):38–62, 2004.
- [50] D. J. DeShazer, R. Breban, E Ott, and R. Roy. Detecting phase synchronization in a chaotic laser array. *Phys. Rev. Lett.*, 87:044101, Jul 2001.

- [51] J. J. Morales-Ruiz. *Differential Galois theory and non-integrability of Hamiltonian systems*. Progress in Mathematics, Birkhauser Verlag, Basel, 1999.
- [52] J. J. Morales-Ruiz. Kovalevskaya, Liapounov, Painlevé, Ziglin and the differential Galois theory. *Regul. Chaotic Dyn.*, 5(3):251–272, 2000.
- [53] K. Yagasaki. Nonintegrability of the unfolding of the fold-Hopf bifurcation. *Nonlinearity*, 31(2):341, 2018.
- [54] P. Acosta-Humánez, M. Alvarez-Ramírez, and T. J. Stuchi. Nonintegrability of the Armbruster–Guckenheimer–Kim quartic Hamiltonian through Morales–Ramis theory. *SIAM J. Appl. Dyn. Syst.*, 17(1):78–96, 2018.
- [55] P. B. Acosta-Humánez, M. Alvarez-Ramírez, and T. J. Stuchi. Nonintegrability of the Armbruster–Guckenheimer–Kim Quartic Hamiltonian Through Morales–Ramis Theory. *J. Applied Dyn. Sys.*, 17(1):78–96, 2018.
- [56] K. Huang, S. Shi, and W. Li. Meromorphic and formal first integrals for the Lorenz system. *J. Nonlin. Math. Phys.*, 25(1):106–121, 2018.
- [57] T. Combot. Integrability of the one dimensional Schrödinger equation. *J. Math. Phys.*, 59(2):022105, 2018.
- [58] C. Mnasri and A.A. Elmandouh. On the dynamics aspects for the plane motion of a particle under the action of potential forces in the presence of a magnetic field. *Results in Phys.*, 9:825 – 831, 2018.
- [59] M. Shibayama. Non-integrability of the spacial n -center problem. *J. Differ. Equations*, 2018.
- [60] A. J. Maciejewski and W. Szumiński. Non-integrability of the semiclassical Jaynes–Cummings models without the rotating-wave approximation. *Appl. Math. Lett.*, 82:132–139, 2018.
- [61] W. Szumiński. Integrability analysis of chaotic and hyperchaotic finance systems. *Nonlinear Dyn.*, 94(1):443–459, 2018.
- [62] A. J. Maciejewski and M. Przybylska. Integrability analysis of the stretch-twist-fold flow. *J. Nonlinear Sci.*, 30(4):1607–1649, 2020.
- [63] W. Szumiński and A. J. Maciejewski. Comment on „Hyperchaos in constrained Hamiltonian system and its control” by J. Li, H. Wu and F. Mei. *Nonlinear Dyn.*, 101:639–654, 2020.
- [64] A. A. Elmandouh. On the integrability of 2D Hamiltonian systems with variable Gaussian curvature. *Nonlinear Dyn.*, 93:933–943, 2018.
- [65] W. Szumiński. On certain integrable and superintegrable weight-homogeneous Hamiltonian systems. *Commun. Nonlinear Sci. Numer. Simulat.*, 67:600–616, 2018.
- [66] W. Szumiński. Integrability analysis of natural Hamiltonian systems in curved spaces. *Commun. Nonlinear Sci. Numer. Simulat.*, 64:246–255, 2018.
- [67] J. J. Kovacic. An algorithm for solving second order linear homogeneous differential equations. *J. Symb. Comput.*, 2(1):461–481, 1986.
- [68] Michael F. Singer and Felix Ulmer. Necessary conditions for Liouvillian solutions of (third order) linear differential equations. *Appl. Algebra Engrg. Comm. Comput.*, 6(1):1–22, 1995.
- [69] Felix Ulmer. Liouvillian solutions of third order differential equations. *Journal of Symbolic Computation*, 36(6):855 – 889, 2003.
- [70] T. Combot and C. Sanabria. A symplectic Kovacic’s algorithm in dimension 4. In *ISSAC’18—Proceedings of the 2018 ACM International Symposium on Symbolic and Algebraic Computation*, pages 143–150. ACM, New York, 2018.
- [71] G. Yakubu, P. Olejnik, and J. Awrejcewicz. Modeling, simulation, and analysis of a variable-length pendulum water pump. *Energies*, 14(23), 2021.

- [72] G. Yakubu, P. Olejnik, and J. Awrejcewicz. On the modeling and simulation of variable-length pendulum systems: A review. *Arch Computat Methods Eng*, 29:2397–2415, 2022.
- [73] P. Olejnik, G. Yakubu, and K. et al Pepa. A double variable-length pendulum with counterweight mass, kinematic excitation and electromagnetic forcing. *Nonlinear Dyn*, 2023.
- [74] F. Ju, Y.S. Choo, and F.S. Cui. Dynamic response of tower crane induced by the pendulum motion of the payload. *Int. J. Solids Struct.*, 43(2):376–389, 2006.
- [75] José Laudelino de Menezes Neto, Gerson Cruz Araujo, Yocelyn Pérez Rothen, and Claudio Vidal. Parametric stability of a double pendulum with variable length and with its center of mass in an elliptic orbit. *J. Geom. Mech.*, 14(3):381–408, 2022.
- [76] J. Freundlich and D. Sado. Dynamics of a coupled mechanical system containing a spherical pendulum and a fractional damper. *Meccanica*, 55:2541–2553, 2020.
- [77] R. Babuska M. Shahbazi and G. A. D. Lopes. Unified modeling and control of walking and running on the spring-loaded inverted pendulum. *IEEE Transactions on Robotics*, 32:1178–1195, 2016.
- [78] *A Simple Spring-Loaded Inverted Pendulum (SLIP) Model of a Bio-Inspired Quadrupedal Robot Over Compliant Terrains*, volume Volume 4B: Dynamics, Vibration, and Control of ASME International Mechanical Engineering Congress and Exposition, 11 2018.
- [79] Raymond H. Plaut and Lawrence N. Virgin. Pendulum models of ponytail motion during walking and running. *J. Sound Vib.*, 332(16):3768–3780, 2013.
- [80] Haowen Yang, Bin Wu, Jinping Li, Yu Bao, and Guoshan Xu. A spring-loaded inverted pendulum model for analysis of human-structure interaction on vibrating surfaces. *J. Sound Vib.*, 522:116727, 2022.
- [81] Hesam Sharghi and Onur Bilgen. Energy harvesting from human walking motion using pendulum-based electromagnetic generators. *J. Sound Vib.*, 534:117036, 2022.
- [82] Marszał M, B. Witkowski, K. Jankowski, P. Perlikowski, and T. Kapitaniak. Energy harvesting from pendulum oscillations. *Int. J. Non-Linear Mech.*, 94:251–256, 2017. A Conspectus of Nonlinear Mechanics: A Tribute to the Oeuvres of Professors G. Rega and F. Vestroni.
- [83] Chun-Hui He, Tarek S Amer, Dan Tian, Amany F Abolila, and Abdallah A Galal. Controlling the kinematics of a spring-pendulum system using an energy harvesting device. *J. Low Freq. Noise Vibr. Act. Control*, 41(3):1234–1257, 2022.
- [84] M.K. Abohamer, J. Awrejcewicz, and T.S. Amer. Modeling of the vibration and stability of a dynamical system coupled with an energy harvesting device. *Alexandria Eng. J.*, 63:377–397, 2023.
- [85] G. Shi, Z. Zhu, Z. H. Zhu, Libration suppression of tethered space system with a moving climber in circular orbit. *Nonlinear Dyn.*, 91:923–937, 2018.
- [86] V. S. Aslanov A double pendulum fixed at the L1 libration point: a precursor to a Mars–Phobos space elevator. *Nonlinear Dyn.*, 112:775–791, 2024.
- [87] D. Bourabah, E. M. Botta Length-rate control for libration reduction during retraction of tethered satellite systems. *Acta Astronaut.*, 201:152–163, 2022.
- [88] E. M. Levin. *Dynamic Analysis of Space Tether Missions*. Univelt Incorporated, San Diego, 2007.
- [89] H. Troger, A. P. Alpatov, V. V. Beletsky, V.I. Dranovskii, V.S. Khoroshilov, A.V. Pirozhenko, A.E. Zakrzhevskii. *Dynamics of Tethered Space Systems*. CRC Press, New York, 2010.
- [90] V. S. Aslanov, A. S. Ledkov. *Dynamics of the Tethered Satellite Systems*. Woodhead Publishing Ltd., Cambridge, England, U. K., 2012.

- [91] V. S. Aslanov and V. Yudinsev Dynamics of large space debris removal using tethered space tug. *Acta Astronaut.*, 91:149–156, 2013.
- [92] A. S. Ledkov, V. S. Aslanov, Evolution of space tethered system’s orbit during space debris towing taking into account the atmosphere influence. *Nonlinear Dyn.*, 96:2211–2223, 2019.
- [93] Z.J. Shahbazzadeh, R. Vatankhah, M. Eghtesad Development and verification of a flexible tethered satellite system model considering the fuel slosh. *Multibody Sys.Dyn.*, 56:289–312, 2022.
- [94] A. K. Misra, M.S. Nixon, V. J. Modi. Nonlinear dynamics of two-body tethered satellite systems: constant length case. *J. Astronaut.*, 49:219–236, 2001.
- [95] D.P. Jin, Z.J. Pang, H. Wen, B.S Yu. Chaotic motions of a tethered satellite system in circular orbit.. *J. Phys. Conf. Ser.*, 744, 012116, 2016.
- [96] V. S. Aslanov, Chaos Behavior of Space Debris During Tethered Tow. *J. J. Guid. Control Dyn.*, 39(10):2399–2405, 2016.
- [97] J. C. Sprott. *Elegant Chaos*. World Scientific, 2010.
- [98] G. Benettin, L. Galgani, A. Giorgilli, and J.-M. Strelcyn. Lyapunov Characteristic Exponents for smooth dynamical systems and for Hamiltonian systems; a method for computing all of them. Parts I and II: Theory and numerical application. *Meccanica*, 15(1):9–20 and 21–30, 1980.
- [99] M. Sandri. Numerical calculation of Lyapunov exponents. *Mathematica J.*, 6:78–84, 1996.
- [100] J. Liouville. Sur la theorie de la variation des constantes arbitraires”. *Journal de mathématiques pures et appliquées.*, 3:342–349, 1838.
- [101] M. J. Lazarotto, I. L. Caldas, and Y. Elskens. Island myriads in periodic potentials. *Chaos: An Interdisciplinary Journal of Nonlinear Science*, 34(3):033115, 03 2024.